Research Square

Preprints are preliminary reports that have not undergone peer review.
They should not be considered conclusive, used to inform clinical practice,
or referenced by the media as validated information.

Self-aligned and self-limiting van der Waals epitaxy of monolayer MoS2 to annihilate grain boundaries for scalable 2D electronics

Yoshiki Sakuma

sakuma.yoshiki@nims.go.jp

Keisuke Atsumi
Takanobu Hiroto
Jun Nara
Akihiro Ohtake
Yuki Ono
Takashi Matsumoto
Emi Kano
Toshiki Yasuno
Xu Yang
Nobuyuki Ikarashi
Asato Suzuki
Michio Ikezawa
Shuhong Li
Tomonori Nishimura
Kaito Kanahashi
Kosuke Nagashio

nagashio@material.t.u-tokyo.ac.jp

Research Article

Keywords:

Posted Date: August 19th, 2025

DOI: https://doi.org/10.21203/rs.3.rs-7386422/v1

License: This work is licensed under a Creative Commons Attribution 4.0 International License.
Read Full License

Additional Declarations: The authors declare no competing interests.

Self-aligned and self-limiting van der Waals epitaxy of monolayer MoS_2 to annihilate grain boundaries for scalable 2D electronics

Yoshiki Sakuma[1*], Keisuke Atsumi[2], Takanobu Hiroto[3], Jun Nara[4], Akihiro Ohtake[1], Yuki Ono[5], Takashi Matsumoto[5], Emi Kano[6], Toshiki Yasuno[6], Xu Yang[6], Nobuyuki Ikarashi[6], Asato Suzuki[7], Michio Ikezawa[7], Shuhong Li[2], Tomonori Nishimura[2], Kaito Kanahashi[2], Kosuke Nagashio[2**]

[1]Research Center for Electronic and Optical Materials, National Institute for Materials Science, 1-1 Namiki, Tsukuba 305-0044, JAPAN

[2]Department of Materials Engineering, The University of Tokyo, 7-3-1 Hongo, Bunkyo-ku, Tokyo 113-8656, Japan

[3]Research Network and Facility Services Division, National Institute for Materials Science, 1-2-1 Sengen, Tsukuba 305-0047, Japan

[4]Research Center for Materials Nanoarchitectonics, National Institute for Materials Science, 1-1 Namiki, Tsukuba 305-0044, JAPAN

[5]Tokyo Electron Technology Solutions Limited, 650 Mitsuzawa, Hosaka-cho, Nirasaki, 407-0192, Japan

[6]Institute of Materials and Systems for Sustainability, Nagoya University, Furo-cho, Chikusa-ku, Nagoya, 464-8601, Japan

[7]Department of Physics, University of Tsukuba, 1-1-1 Tennodai, Tsukuba, 305-8571, Japan

*sakuma.yoshiki@nims.go.jp, **nagashio@material.t.u-tokyo.ac.jp

Abstract

Toward future logic semiconductors at sub-1 nm nodes, unidirectional nucleation followed by seamless stitching has emerged as an exclusive strategy for scalable epitaxial growth of single-crystalline monolayer transition metal dichalcogenides on sapphire substrates. In contrast, here we present a novel growth mechanism for single-crystalline MoS_2 on c-plane sapphire via metal-organic chemical vapor deposition (MOCVD). The initial nucleation generates not only 0° and antiparallel 60° domains but also low-angle twisted domains, consistent with the coincidence site lattice framework. Nevertheless, these rotationally misoriented domains are deterministically self-aligned and merged into energetically preferred 0° domain during coalescence, yielding a continuous, unidirectional single-crystal. Additionally, by employing MoO_2Cl_2 as a molybdenum precursor, MoS_2 grows in a self-limiting manner. This epitaxial strategy is substantiated by phonon-limited mobility of 66 cm^2/Vs at room temperature and 749 cm^2/Vs at low temperatures. Our approach offers a practical and reproducible scheme for MOCVD-based van der Waals epitaxy in 2D electronics.

To fully exploit two-dimensional (2D) transition metal dichalcogenides (TMDCs) for future logic semiconductors at sub-1 nm nodes,[1] owing to their inherent immunity against short-channel effects, scalable epitaxial growth techniques for single-crystalline monolayer TMDC films are in critical demand.[2,3] From an industrial perspective, realizing 2D materials on a wafer scale requires prioritized development of quasi-van der Waals (vdW) epitaxy on large 3D crystalline substrates such as sapphire (α-Al_2O_3), which exhibits superior crystalline quality, exceptional chemical, thermal stability, as well as proven scalability to 300 mm in diameter.[4]

Since c-plane of bulk sapphire exhibits C_{3v} symmetry, whereas monolayer MoS_2, for instance, possesses D_{3h} symmetry with a three-fold rotational axis, it should, in principle, undergo heteroepitaxial growth with unidirectional in-plane crystallographic orientation on c-

plane sapphire.[5] Nonetheless, early studies that concentrated solely on the symmetry of both MoS_2 and c-plane sapphire led to the inevitable formation of antiparallel domains,[6] rendering unidirectional growth challenging to realize. To address this obstacle, two major strategies known as step-edge-guided and symmetry-guided epitaxy have been proposed. Specifically, in the step-edge-guided mode,[7] the step edges help to lower the surface symmetry to C_1 and break the degeneracy of nucleation energy between twined islands, guiding their in-plane orientation along a single preferred direction. In contrast, the crucial role of atomic symmetry at the terrace surface is highlighted in the symmetry guided epitaxy. A single-type O-Al atomic slab structure with even number of surface steps on c-plane sapphire, which was exposed by deliberately engineered miscut angles, strongly facilitates unidirectional growth of MoS_2.[8] Consequently, some studies have successfully demonstrated the unidirectionally aligned TMDC films on sapphire substrates by employing techniques such as powder-source chemical vapor deposition (CVD),[7–13] metal-organic CVD (MOCVD)[14,15] and other techniques.[16]

However, although both mechanisms are conceptually plausible, their underlying atomistic processes remain elusive. This lack of clarity arises from unresolved questions regarding the surface reconstructions[14,17] and chemical adsorbates on sapphire in growth environment, the atomic configurations of sapphire step edges,[7,8] and the edge terminations of TMDC grains.[18,19] Moreover, it has been reported that the sulfur to metal precursor supply ratio,[13,20–22] along with the introduction of H_2,[23] influences the in-plane alignment of TMDC nuclei on sapphire. In fact, these growth conditions can be utilized to underscore and control the favored growth mode separately. Conversely, this implies that both mechanisms inherently coexist in the growth on the same vicinal sapphire surface.

Moreover, the formation of various interfacial layers on sapphire surfaces[15,24,25] has also been identified as playing a critical role in determining the in-plane crystallographic orientations of MoS_2. Notably, the underlying mechanism responsible for the emergence of

MoS_2 with two distinct orthogonal configurations on c-plane sapphire (0°/60° and 30°/90°) under different experimental conditions remains to be fully elucidated. These complexities impede a comprehensive and unified understanding of quasi-vdW growth mechanism at nucleation stage, particularly pronounced in MOCVD-based research due to limited investigations. Nonetheless, it should be emphasized that all the above-mentioned studies are based on a common strategy, in which aligning all the nuclei in the same in-plane orientation and subsequent seamless stitching are regarded as a guiding principle,[26] as depicted in **Figure 1a**.

In this study, unlike the conventional strategy, we report a fundamentally distinct and previously unobserved self-aligned coalescence mechanism for wafer-scale single-crystalline MoS_2 films in an MOCVD-type reactor using MoO_2Cl_2 and H_2S as precursors, as shown in **Figure 1a** and **Supplementary Fig. S1**. Besides antiparallel nuclei, isolated MoS_2 domains initially nucleated with well-defined in-plane twisted angles elucidated by coincidence site lattice (or supercell) model between MoS_2 and sapphire. Subsequently, upon domain impingement, both the low-angle and antiparallel 60° domains are self-aligned and merged into the most energetically favorable 0° domain during coalescence process. Consequently, only the 0° domain survives, culminating in a deterministic formation of continuous, unidirectionally aligned single-crystalline MoS_2 film. Another noticeable feature of MoS_2 growth using MoO_2Cl_2 precursor is a self-limiting manner over a wide range of growth conditions. As a proof of high quality MoS_2 films with negligible grain boundaries, carrier transport exhibited phonon-limited behavior, yielding record high electron mobilities of 66 cm^2/Vs at room temperature and approximately 749 cm^2/Vs at low temperatures.

Epitaxial registry, self-aligned coalescence and annihilation of grain boundaries

An industrially compatible c-plane sapphire substrate with an orientation flat plane of

($\bar{1}\bar{1}20$) and a miscut angle of 0.15° - 0.2° toward m-axis of [$1\bar{1}00$] direction (notated as c/m: -0.15° or 0.2°), manufactured by Orbray Co. Ltd., was utilized as a standard substrate in this study. Prior to growth, the substrate was annealed in air for 1 hour at 1150°C to form parallel monolayer atomic steps along a-axis of [$11\bar{2}0$] with a terrace width of approximately 80-60 nm (**Supplementary Fig. S2**).[27] Monolayer MoS_2 films were grown via MOCVD reactor, utilizing MoO_2Cl_2 and H_2S as precursors in N_2 carrier gas. Growth temperatures ranged from 800°C to 1050°C, with a maximum growth duration of 2 hours (see **Methods**). Notably, MoO_2Cl_2 precursor not only exhibits adequate volatility comparable to that of conventional $Mo(CO)_6$ around room temperature, but also the advantage of eliminating carbon contamination.[28] At a growth temperature of 950°C and a duration of 30 min, isolated MoS_2 domains were clearly observed, as shown in **Figure 1b**. These domains comprised antiparallel triangular domains of 0° and 60°, approximately 150 nm in size, oriented along [$1\bar{1}00$] and [$\bar{1}100$], respectively. About ~55% of domains exhibited 0° and the remainder was 60°. Upon closer inspection, however, ~11° and ~49° domains were also discerned, as shown by blue dotted lines. Extending the growth duration to 60 min resulted in a fully continuous monolayer MoS_2 film. It is noteworthy that the terrace width of the sapphire surface increased significantly[14] probably due to the highly reactive nature of H_2S gas at elevated temperatures exceeding 950°C. For the fully-covered sample, the epitaxial relationship of [$11\bar{2}0$]MoS_2//[$11\bar{2}0$]α-Al_2O_3 was confirmed through in-plane X-ray diffraction (XRD) ϕ scans (**Supplementary Fig. S3**), which is consistent with the previous literature for MoS_2 growth on sapphire substrates by MOCVD[17,29] and powder CVD.[6,21,30]

We performed a detailed analysis of the orientational relationships between the MoS_2 and sapphire substrate for isolated domains grown at 975°C for 20 min. As depicted in **Supplementary Fig. S4**, high-resolution in-plane XRD measurement revealed the presence of additional subpeaks at azimuthal angles of approximately 11°, 19°, 30°, 41° and 49° between

the principal peaks at 0° and 60°, which are equivalent to 0°±11°, 30°±11°. Although some of these subpeaks were also reported previously, their origin and implications have yet to be apparently elucidated.[31] The observed azimuthal angles exhibit excellent agreement with those derived from supercells between the commensurate MoS_2 and c-plane sapphire substrate, as detailed in the table of **Supplementary Fig. S4**.[6] Moreover, the subpeak with 10.89° twisted angle was resolved into a doublet at 10.4° and 11.3° (average: 10.85°), although the underlying mechanism remains unclear. Notably, the prominent peaks at 0° and ~10.85° with large XRD intensities correspond to the two smallest supercell sizes in the table, suggesting that the epitaxial registry of tiny nuclei at the early stage of MoS_2 growth is likely governed by coincidence site lattice model.

The time evolution of MoS_2 growth at 975°C was systematically examined to elucidate the pathway to full surface coverage, as depicted in **Supplementary Fig. S5**. **Figure 1c** overlays the data corresponding to the 0° domain at different growth durations, highlighting the correlation between primary 0° peak and doublet 10.4°/11.3° subpeaks. Intriguingly, the intensity of these doublet peaks initially exhibited a monotonic increase with the growth duration, followed by a rapid decrease around 50 min, ultimately vanishing altogether. Concurrently, a broad tail structure at the foot of the 0° peak emerged at approximately 40 min, and dissipated by 60 min. Throughout this process, the area intensity of the primary 0° peak exhibited a continuous increase, as shown in the inset of **Figure 1c**. To attain the real-space observation of this newly found coalescence processes, novel techniques using differential dark-field transmission electron microscopy (DF-TEM) analysis were developed. While in-plane XRD lacks the sensitivity to unambiguously resolve antiparallel domains of 0° and 60°, electron diffraction techniques are capable of their clear differentiation.[32] Although Friedel's law describes that the intensities of *hkl* and *-h-k-l* reflections are equivalent even for polar crystals, this equivalence is violated in monolayer TMDCs owing to the broken in-plane

inversion symmetry and multiple scattering effects, resulting in anomalous diffraction intensity contrasts.[33] As shown in **Supplementary Fig. S6**, therefore, by taking the difference between DF-TEM images obtained from a pair of diffraction spots related by 180° inversion, where Friedel's law is violated, 0° and 60° antiparallel domains are unambiguously distinguished. Moreover, comparison with the corresponding bright-field (BF) TEM image allows for the discrimination of low-angle twisted domains in addition to the 0° and 60° antiparallel domains, thereby enabling the construction of comprehensive false-color maps for monolayer MoS_2 grown at 975°C for various growth durations, as shown in **Figure 1d**. At 35 min, nearly all domains retain their triangular morphology and a substantial fraction of both 60° antiparallel and low-angle twisted domains clearly remains. Interestingly, at 45 min, 60° antiparallel domains as well as low-angle twisted domains, which was observed in in-plane XRD, are significantly reduced due to coalescence and almost annihilated by 60 min, resulting in the fully covered single-crystalline MoS_2 film. Such systematic time evolution is uniquely accessible through the highly reproducible nature of MOCVD growth, whereas acquiring such detailed and consistent data is exceedingly difficult with conventional powder-source CVD.

These observations strongly indicate the following scenario. In the early stage of growth, small nuclei formed independently while maintaining their twisted angles elucidated by supercell model. Upon impingement of the domains in lateral at approximately 40 min, the low-angle twisted domains, followed by the antiparallel 60° domains, started to merge into the energetically favorable 0°domain to form a single crystal via the self-aligned seamless stitching. Finally, complete surface coverage was attained by 60 min. Here, it is important to note that, using the time-resolved in-plane XRD, this time evolution was also observed at a reduced temperature of 950°C (**Supplementary Fig. S7**) and even with alternative precursors of $Mo(CO)_6$ and H_2S at 950°C (**Supplementary Fig. S8**), suggesting that the formation of single crystals via merging and seamless stitching following the impingement is a generalizable

phenomenon, not limited to the MoO_2Cl_2 precursor.

To further gain profound insights into the coalescence process of MoS_2 grains in fully continuous films grown at different temperatures, four-dimensional-scanning transmission electron microscopy (4D-STEM)[29,34] and polarization-resolved second harmonic generation (SHG)[35] was utilized to visualize the orientation of grains at the multiple spatial resolutions from nanometer to micrometer, as illustrated in **Figure 1e**, **1f** and **Supplementary Figs. S9-S10**. As the growth temperature increases, the low-angle twisted domains and antiparallel domains, initially incorporated into the dominant 0° domains at 900°C, were significantly reduced, eventually disappearing almost entirely at 975°C. These observations strongly suggest that a relatively high temperature of 975°C is critical for achieving complete single-crystal formation via self-aligned coalescence. Moreover, SHG is highly sensitive to strain levels as low as 0.1%, which remain undetectable by Raman spectroscopy.[36] The polar plot of the parallel SHG component for MoS_2 grown at 975°C reveals a uniform six-fold symmetry with maximum intensity along the armchair direction, confirming the absence of substantial residual strain in the film.

Deterministic epitaxial alignment of MoS_2/sapphire

The novel phenomenon of single-crystal formation via self-aligned coalescence, as observed in **Figure 1d**, suggests the existence of a deterministic crystallographic orientation of MoS_2 on the sapphire substrate. **Figure 2a** presents a cross-sectional high-angle annular dark field scanning TEM (HAADF-STEM) image of MoS_2 grown on the sapphire substrate at 975°C, observed from the $[11\bar{2}0]$ direction. The r$(1\bar{1}02)$, R$(\bar{1}104)$, and m$(1\bar{1}00)$ faces of the sapphire substrate were clearly discerned, corroborating the crystallographic asymmetry along +m$[\bar{1}100]$ and -m$[1\bar{1}00]$, *i.e.* the threefold symmetry of sapphire, depicted in the inset. Although a vdW MoS_2/sapphire distance was observed as ~0.7 nm for bottom S-top Al

distance,[7,8,13,25] the precise in-plane atomic alignment of MoS_2 on the sapphire substrate remained unclear. To clarify this, low-energy electron diffraction (LEED) measurements were performed for monolayer MoS_2 grown on the standard sapphire substrate (c/m = -0.2°) at 975°C at specific voltage of 190 eV across eight positions, each spaced 1 mm apart. As shown in **Figure 2b** and **Supplementary Fig. S11**, all exhibited a consistent threefold symmetric diffraction pattern of single-crystalline monolayer MoS_2,[7,13] indicating the uniform alignment of MoS_2 on a wafer scale. Furthermore, the atomic configuration of monolayer MoS_2 on the sapphire substrate was determined by analyzing the LEED intensity - voltage (*I-V*) profiles from 10 and 01 LEED spots. It was revealed that the MoS_2 structural model shown in **Figure 2c** can be directly overlaid onto the sapphire substrate schematically drawn. Additionally, when monolayer MoS_2 was grown on a custom-ordered sapphire substrate with an opposite miscut angle of +0.2° along the m-direction (c/m = +0.2°), as shown in **Supplementary Fig. S12**, identical LEED patterns were obtained irrespective of the miscut direction, as shown in **Figure 2c**. Given the inherent threefold symmetry of the c-sapphire top-most surface, the disparity in the miscut direction results in a difference in the atomic structure at the step edges. Therefore, it can be concluded that the orientation of MoS_2 during the MOCVD growth is governed not by the step edges but by its interaction with the surface structure of the sapphire substrate. Thus, the orientation of MoS_2 on the sapphire substrate grown at 975°C is uniquely determined, with the MoS_2 $[11\bar{2}0]$ and $[\bar{1}100]$ directions aligning with the sapphire $[11\bar{2}0]$ and $[\bar{1}100]$ directions, respectively. MoS_2 with this orientation is indeed the 0° domain depicted in **Figure 2c**. It should be noted that this configuration matches that reported in previous growth studies (0°/60°),[6] while differing from the orientation relationships observed in other reports (30°/90°).[7,8,13,37] As mentioned in the *introduction*, this may be related to specific interfacial and buffer layers on sapphire surface caused by the precursor supply ratio (S/Mo).[12,21,22]

Subsequently, we aim to explore the mechanism by which low-angle and antiparallel

domains are annihilated. As illustrated in **Figure 2d**, two mechanisms can be considered: the rotation model and the grain boundary (GB) migration model. In general, the rotation of antiparallel grains in opposite orientation might be possible in vdW heteroepitaxy due to the weak interaction.[38] However, time-resolved differential DF-TEM images in **Figure 1d** clearly indicate that there is inadequate space to accommodate the rotation process when coalescence initiates ~40 minutes after the commencement of growth. In contrast, GB migration model involves mass transfer between adjacent grains across the boundary via atomic diffusion within the solid, without requiring additional spatial allowance. When low-angle and antiparallel domains are in physical contact with 0° domains, the movement of Mo and S atoms, facilitated by vacancies and interstitials, will drive GB migration. Therefore, a diffusion-coupled GB migration model is the most plausible explanation. Additional discussion is provided in **Supplementary Fig. S13**.

This type of orientation-selective growth process is classically recognized as epitaxial grain growth (EGG) in polycrystalline thin films on single crystalline substrates.[39] EGG is driven by the minimization of crystallographically anisotropic free energies, such as surface and interface energies. At the monolayer limit of 2D materials, as discussed in **Supplementary Fig. S14**, MoS_2/sapphire interface energy is expected to play a dominant role. Therefore, to elucidate the driving force, density functional theory (DFT) calculations were conducted to compute the adsorption energies between the MoS_2 and sapphire substrate at various twisted angles, assuming commensurate infinite monolayer MoS_2 slabs, as shown in **Supplementary Fig. S15**. **Figure 2e** summarizes the relative adsorption stabilities of the 0°, antiparallel, and low-angle twisted domains. In isolation from the substrate, all domains are energetically equivalent. However, upon impingement, the merging of 10.9° domains into 0° domains is driven by an adsorption energy difference of ΔE_{ad} = 35 meV/MoS_2 unit via the GB migration. On the other hand, ΔE_{ad} between 0 and 60 antiparallel domains should exist but was negligibly

small (~0.1 meV/MoS_2 unit), indicating that the grain boundary energy must be considered in further studies, as discussed in **Supplementary Fig. S14**. Nevertheless, it is important to emphasize that even such small energy differences can induce GB migration, as reported for adjacent graphene islands on Ir(111), where the driving force was on the order of 0.1 meV per C atom.[38] The present energy considerations are supported by the differential DF-TEM and 4D-STEM observations (**Figure 1d** and **Supplementary Fig. S10**).

Wafer scale uniformity via self-limiting growth

To guarantee the reliable performance of electronic devices whose properties are highly sensitive to the precise number of 2D material layers, self-limited layer-controlled synthesis provides great technical advantages. While atomic layer deposition (ALD) is among the most promising techniques owing to its surface adsorbed growth mechanism, substantial progress is still required to enhance the crystallinity of MoS_2 films.[40,41] In the epitaxial growth of TMDC on the sapphire substrate via MOCVD, precise layer control remains a significant challenge, primarily due to the nonuniform gas flow pattern across wafer surface and the consumption of precursors along the gas flow direction in reactor.[24,42,43] Here, although the MoO_2Cl_2 and H_2S precursors were supplied simultaneously, unlike ALD, a self-limited monolayer growth of MoS_2 was demonstrated as shown in **Figure 3a** and **Supplementary Fig. S16**. The absorbance at C exciton measured for MoS_2 films, grown on double-side polished sapphire substrates at 850°C, saturates beyond 60 min, in contrast to the continuous growth tendency observed using $Mo(CO)_6$ and H_2S precursors. Moreover, the self-limiting growth is rather profound at an elevated temperature of 975°C under optimized growth conditions, as shown in **Supplementary Fig. S17**. This is supported by atomic force microscope (AFM) images in **Figure 3b**, where no voids and very limited second layer growth of MoS_2 are discernable even at the longer growth duration of 90 min. Moreover, the tail of main XRD peak at 0° in **Figure**

1c and **Supplementary Fig. S9** no longer broadens for MoO_2Cl_2, while broad tail behavior observed due to the mosaic spread caused by the second epitaxial layer of MoS_2 for $Mo(CO)_6$ in **Supplementary Fig. S8**. The mechanism of this self-limiting is attributed to site-selective adsorption, wherein the MoO_2Cl_2 precursor, unlike $Mo(CO)_6$, exhibits a low affinity for adsorption on the MoS_2 surface. The detailed discussion can be found in **Supplementary Fig. S17**.

This self-limited layer-controlled synthesis enables wafer-scale uniformity in MoS_2 growth, as shown by a 2-inch monolayer MoS_2/c-sapphire substrate in **Figure 3c**. The quality and uniformity of the as-grown monolayer MoS_2 films are illustrated via multi-scale characterizations. High-resolution in-plane XRD ϕ scans at five different points in the wafer, as shown in **Figure 3d**, macroscopically revealed the formation of uniform film without low-angle and antiparallel domains throughout the wafer. The variation in Raman A_{1g} peaks of the monolayer MoS_2 is only 2 cm^{-1} throughout the 2-inch wafer, as shown in **Figure 3e**. Moreover, **Figure 3f** shows photoluminescence (PL) line scans across a 2-inch MoS_2 wafer with 2 mm step. No obvious variations in peak position and line width were observed. These results collectively demonstrate the excellent uniformity and high reproducibility of MOCVD-grown MoS_2 films, spanning from the sub-micrometer to centimeter scale.

Phonon limited electron mobility

To evaluate the electronic performance of monolayer MoS_2, Hall bar and two-terminal field-effect transistor (FET) configurations were prepared via a standard photolithography process after transferring MoS_2 to a SiO_2/Si substrate, as shown in **Figure 4a** and **Supplementary Fig. S18**. **Figures 4b** exhibit transfer curves with limited variation obtained from MoS_2 grown at 1025°C, showing the on/off current ratio exceeding ~10^7 and clear saturation. **Figure 4c** shows output characteristics obtained from MoS_2 grown at 975°C, showing ohmic behavior using

Ni/Au contacts. The primary focus is placed on the temperature dependence of mobility (μ),[44,45] rather than its absolute value, as the mobilities achieved via MOCVD are comparatively lower than those obtained using powder CVD,[2] rendering small comparisons of μ values at room temperature less meaningful. **Figure 4d** and **Supplementary Fig. S19** summarize the μ values as a function of temperature for MoS_2 grown under different conditions. As the growth temperature increases from 900°C to 1025°C, a marked transition from thermally activated behavior to phonon-limited behavior occurs.[44] The temperature-dependent μ for MoS_2 grown at 1025°C attains a record-high mobility, approximately 66 cm^2/Vs at room temperature and 749 cm^2/Vs at 20 K, for monolayer MoS_2 synthesized by MOCVD. Furthermore, this temperature dependence approaches values similar to those achieved previously with powder CVD,[46] where large single-crystal triangles have been measured, strongly indicating the single crystal formation by the annihilation of GBs. It is noteworthy that MoS_2 properties were characterized on 2 cm^2 sapphire wafers, while devices were fabricated using 2-inch wafers. The 2-inch wafers require ~50°C higher substrate temperatures due to different MOCVD susceptors. The μ values of two-terminal MoS_2 FETs in **Figure 4e** show that the average room-temperature μ increases with increasing growth temperatures. Finally, **Figure 4f** benchmarks the maximum and average μ values at room temperature, with the current study reporting the highest value to date.

Conclusion

In this study, we have revealed a self-aligned and self-limiting vdW epitaxy for unidirectional single-crystalline MoS_2 film on c-plane sapphire, by employing high-precision, time-resolved in-plane XRD, differential DF-TEM and 4D-STEM. The epitaxial relationship between MoS_2 and sapphire substrate was deterministically elucidated, with the MoS_2 $[11\bar{2}0]$ and $[\bar{1}100]$ directions aligning with the sapphire $[11\bar{2}0]$ and $[\bar{1}100]$ directions, respectively. Our results

demonstrate the superiority of MOCVD technology in growing monolayer TMDCs, providing a major impetus for future industrialization.

References

1. Cao, W. *et al.* The future transistors. *Nature* **620**, 501–515 (2023).
2. Wu, P., Zhang, T., Zhu, J., Palacios, T. & Kong, J. 2D materials for logic device scaling. *Nat Mater* **23**, 23–25 (2024).
3. Liu, C. *et al.* Understanding epitaxial growth of two-dimensional materials and their homostructures. *Nat Nanotechnol* **19**, 907–918 (2024).
4. Akselrod, M. S. & Bruni, F. J. Modern trends in crystal growth and new applications of sapphire. in *Journal of Crystal Growth* **360** 134–145 (2012).
5. Dong, J., Zhang, L., Dai, X. & Ding, F. The epitaxy of 2D materials growth. *Nat Commun* **11**, (2020).
6. Dumcenco, D. *et al.* Large-area epitaxial monolayer MoS_2. *ACS Nano* **9**, 4611–4620 (2015).
7. Li, T. *et al.* Epitaxial growth of wafer-scale molybdenum disulfide semiconductor single crystals on sapphire. *Nat Nanotechnol* **16**, 1201–1207 (2021).
8. Fu, J. H. *et al.* Oriented lateral growth of two-dimensional materials on c-plane sapphire. *Nat Nanotechnol* **18**, 1289–1294 (2023).
9. Wang, J. *et al.* Dual-coupling-guided epitaxial growth of wafer-scale single-crystal WS_2 monolayer on vicinal a-plane sapphire. *Nat Nanotechnol* **17**, 33–38 (2022).
10. Liu, L. *et al.* Uniform nucleation and epitaxy of bilayer molybdenum disulfide on sapphire. *Nature* **605**, 69–75 (2022).
11. Chang, Y. *et al.* Atomically thin decoration layers for robust orientation control of 2D transition metal dichalcogenides. *Adv Funct Mater* **34**, 2311387 (2024).
12. Zheng, P. *et al.* Universal epitaxy of non-centrosymmetric two-dimensional single-crystal metal dichalcogenides. *Nat Commun* **14**, 592 (2023).
13. Li, L. *et al.* Epitaxy of wafer-scale single-crystal MoS_2 monolayer via buffer layer control. *Nat Commun* **15**, 1825 (2024).
14. Chubarov, M. *et al.* Wafer-scale epitaxial growth of unidirectional WS_2 monolayers on sapphire. *ACS Nano* **15**, 2532–2541 (2021).
15. Zhu, H. *et al.* Step engineering for nucleation and domain orientation control in WSe_2 epitaxy on c-plane sapphire. *Nat Nanotechnol* **18**, 1295–1302 (2023).
16. Yang, P. *et al.* Highly reproducible epitaxial growth of wafer-scale single-crystal monolayer MoS_2 on sapphire. *Small Methods* **7**, 2300165 (2023).
17. Park, Y. *et al.* Critical role of surface termination of sapphire substrates in crystallographic epitaxial growth of MoS_2 using inorganic molecular precursors. *ACS Nano* **17**, 1196–1205 (2023).
18. Lauritsen, J. V. *et al.* Size-dependent structure of MoS_2 nanocrystals. *Nat Nanotechnol* **2**, 53–58 (2007).

19. Hansen, L. P. *et al.* Atomic-scale edge structures on industrial-style MoS_2 nanocatalysts. *Angewandte Chemie - International Edition* **50**, 10153–10156 (2011).
20. Aljarb, A. *et al.* Substrate lattice-guided seed formation controls the orientation of 2D transition-metal dichalcogenides. *ACS Nano* **11**, 9215–9222 (2017).
21. Suenaga, K. *et al.* Surface-mediated aligned growth of monolayer MoS_2 and in-plane heterostructures with graphene on sapphire. *ACS Nano* **12**, 10032–10044 (2018).
22. Li, C. *et al.* Revisiting the epitaxial growth mechanism of 2D TMDC single crystals. *Advanced Materials* **36**, 2404923 (2024).
23. Ji, H. G. *et al.* Hydrogen-assisted epitaxial growth of monolayer tungsten disulfide and seamless grain stitching. *Chemistry of Materials* **30**, 403–411 (2018).
24. Lin, Y. C. *et al.* Realizing large-scale, electronic-grade two-dimensional semiconductors. *ACS Nano* **12**, 965–975 (2018).
25. Xiang, Y. *et al.* Monolayer MoS_2 on sapphire: an azimuthal reflection high-energy electron diffraction perspective. *2D Mater* **8**, 025003 (2021).
26. Zhang, L., Dong, J. & Ding, F. Strategies, status, and challenges in wafer scale single crystalline two-dimensional materials synthesis. *Chem Rev* **121**, 6321–6372 (2021).
27. Curiotto, S. & Chatain, D. Surface morphology and composition of c-, a- and m-sapphire surfaces in O_2 and H_2 environments. *Surf Sci* **603**, 2688–2697 (2009).
28. Yang, X., Li, S., Ikeda, N., Ohtake, A. & Sakuma, Y. Scalable growth of atomically thin MoS_2 layers in a conventional MOCVD system using molybdenum dichloride dioxide as the molybdenum source. *Appl Surf Sci* **636**, 157756 (2023).
29. Chen, C. *et al.* Effect of growth temperature on the microstructure and properties of epitaxial MoS_2 monolayers grown by metalorganic chemical vapor deposition. *Journal of Vacuum Science & Technology A* **42**, 022201 (2024).
30. Yu, H. *et al.* Wafer-scale growth and transfer of highly-oriented monolayer MoS_2 continuous films. *ACS Nano* **11**, 12001–12007 (2017).
31. Chubarov, M., Choudhury, T. H., Zhang, X. & Redwing, J. M. In-plane x-ray diffraction for characterization of monolayer and few-layer transition metal dichalcogenide films. *Nanotechnology* **29**, 055706 (2018).
32. Van Der Zande, A. M. *et al.* Grains and grain boundaries in highly crystalline monolayer molybdenum disulphide. *Nat Mater* **12**, 554–561 (2013).
33. Deb, P. *et al.* Imaging polarity in two dimensional materials by breaking Friedel's law. *Ultramicroscopy* **215**, 113019 (2020).
34. Han, Y. *et al.* Strain mapping of two-dimensional heterostructures with subpicometer precision. *Nano Lett* **18**, 3746–3751 (2018).
35. Li, Y. *et al.* Probing symmetry properties of few-layer MoS_2 and *h*-BN by optical second-harmonic generation. *Nano Lett* **13**, 3329–3333 (2013).
36. Mennel, L. *et al.* Optical imaging of strain in two-dimensional crystals. *Nat Commun* **9**, 516 (2018).

37. Ahn, H. *et al.* Integrated 1D epitaxial mirror twin boundaries for ultrascaled 2D MoS_2 field-effect transistors. *Nat Nanotechnol* **19**, 955–961 (2024).
38. Rogge, P. C. *et al.* Real-time observation of epitaxial graphene domain reorientation. *Nat Commun* **6**, 6880 (2015).
39. Thompson, C. V. Grain Growth in thin films. *Annu. Rev. Mater. Sci.* **20**, 245–268 (1990).
40. Tan, L. K. *et al.* Atomic layer deposition of a MoS_2 film. *Nanoscale* **6**, 10584–10588 (2014).
41. Jurca, T. *et al.* Low-temperature atomic layer deposition of MoS_2 films. *Angewandte Chemie* **129**, 5073–5077 (2017).
42. Smets, Q. *et al.* Sources of variability in scaled MoS_2 FETs. *2020 IEEE International Electron Devices Meeting (IEDM)* **December**, 3.1.1-3.1.4 (2020).
43. Shi, Y. *et al.* Engineering wafer-scale epitaxial two-dimensional materials through sapphire template screening for advanced high-performance nanoelectronics. *ACS Nano* **15**, 9482–9494 (2021).
44. Yu, Z. *et al.* Towards intrinsic charge transport in monolayer molybdenum disulfide by defect and interface engineering. *Nat Commun* **5**, 1–7 (2014).
45. Cui, X. *et al.* Multi-terminal transport measurements of MoS_2 using a van der Waals heterostructure device platform. *Nat Nanotechnol* **10**, 534–540 (2015).
46. Kurabayashi, S. & Nagashio, K. Transport properties of the top and bottom surfaces in monolayer MoS_2 grown by chemical vapor deposition. *Nanoscale* **9**, 13264–13271 (2017).
47. Chang, H.-Y., Zhu, W. & Akinwande, D. On the mobility and contact resistance evaluation for transistors based on MoS_2 or two-dimensional semiconducting atomic crystals. *Appl Phys Lett* **104**, 113504 (2014).
48. Zhu, J. *et al.* Low-thermal-budget synthesis of monolayer molybdenum disulfide for silicon back-end-of-line integration on a 200 mm platform. *Nat Nanotechnol* **18**, 456–463 (2023).

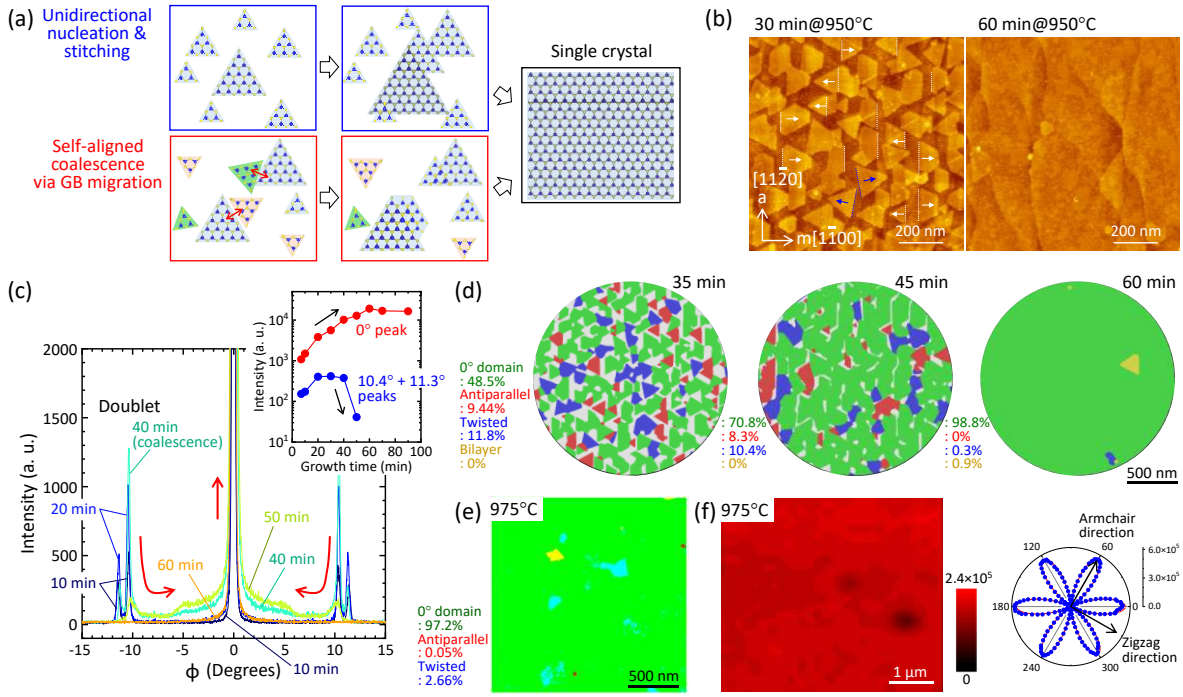

Fig. 1| Annihilation of antiparallel & low-angle twisted domains during coalescence of MoS_2 domains on sapphire substrates. a, Schematic illustration of two kinds of growth strategies for the single crystal formation. **b**, AFM images of MoS_2 grown on the sapphire substrate at 30 and 60 min at 950°C. **c**, in-plane XRD intensity around the 0° peak for the ϕ scan of MoS_2 acquired at different growth durations at 975°C. The inset shows the intensities of XRD peaks at 0° and ~11° as a function of growth durations. The sum of the intensity of doublet subpeaks at 10.4° and 11.3° was plotted as ~11°. **d**, False-color maps obtained by time-resolved differential DF-TEM analysis of MoS_2 grown at 975°C. The proportion of each domain was calculated based on the absolute coverage. **e**, 4D-STEM data of MoS_2 grown at 975°C. **f**, SHG intensity map and typical polarization dependence of SHG for MoS_2 grown at 975°C.

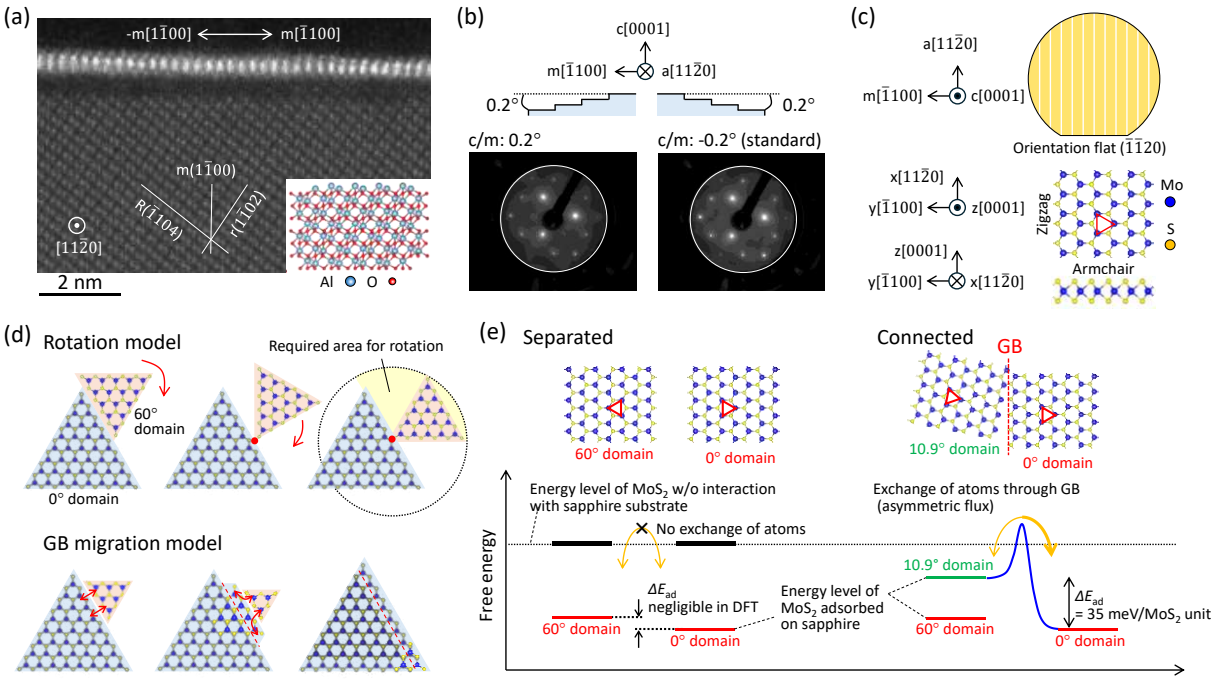

Fig. 2| Determination of unique MoS_2/sapphire orientation & growth mechanism. a, Cross-sectional HAADF-STEM image of monolayer MoS_2 grown on the sapphire substrate at 975°C. **b**, LEED patterns of MoS_2 grown on sapphire substrates with opposing miscut angles. **c**, Definition of orientation for the sapphire substate and monolayer MoS_2. Note that the orientation of monolayer MoS_2 is defined by the bottom layer of the unit cell, as specified in the standard crystallographic information (cif) file. **d**, Illustration of two distinct growth mechanisms. **e**, Schematic representation of the energy relationship between the 0°, 10.9° and 60° domains with adsorption energy differences calculated by DFT.

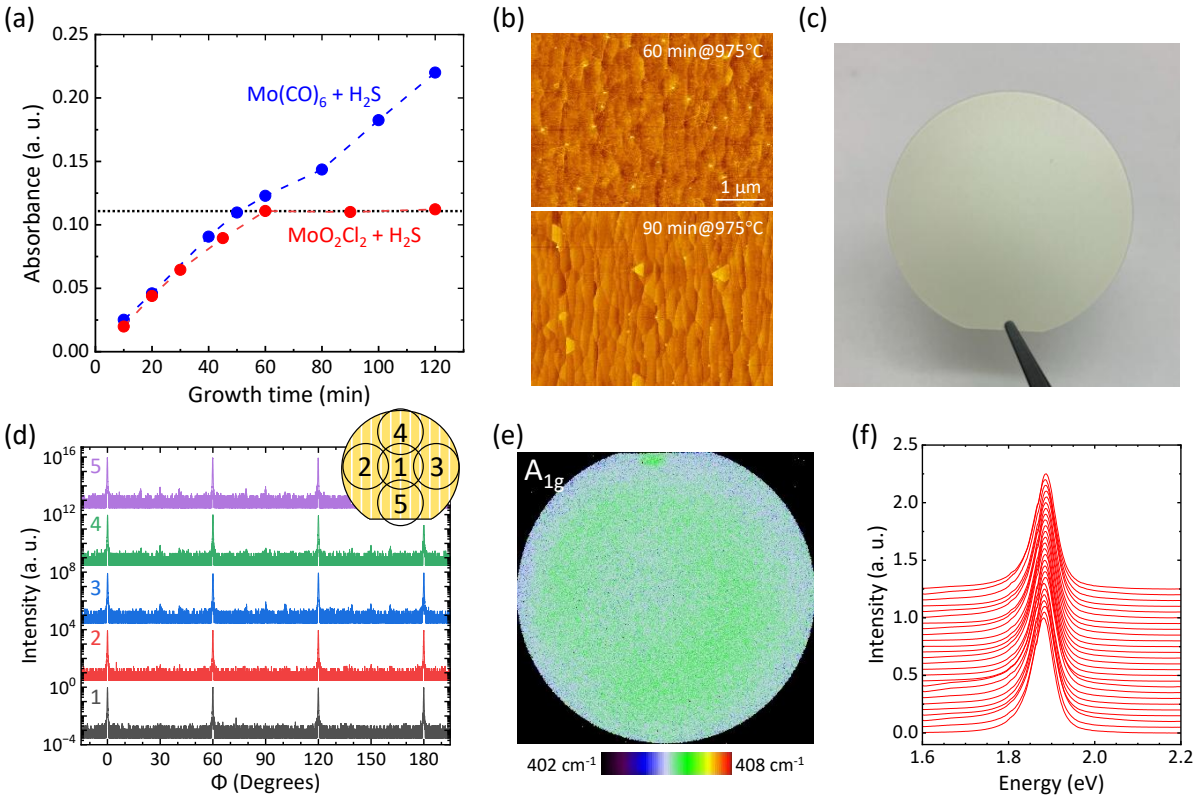

Fig. 3| Wafer scale uniformity via self-limiting growth. a, Absorbance of MoS_2 grown on sapphire substrates at 850°C as a function of growth durations using different precursors. **b**, AFM images of MoS_2 grown on sapphire substrates at 975°C at various growth durations. **c**, Photograph of a 2-inch monolayer MoS_2/c-sapphire substrate. **d**, In-plane XRD ϕ scans taken at five different locations for monolayer MoS_2 grown on a 2-inch sapphire substrate at 950°C. **e**, Raman A_{1g} intensity map for monolayer MoS_2 grown on a 2-inch sapphire substrate at 850°C. **f**, PL line scans along the wafer for monolayer MoS_2 grown on a 2-inch sapphire substrate at 950°C.

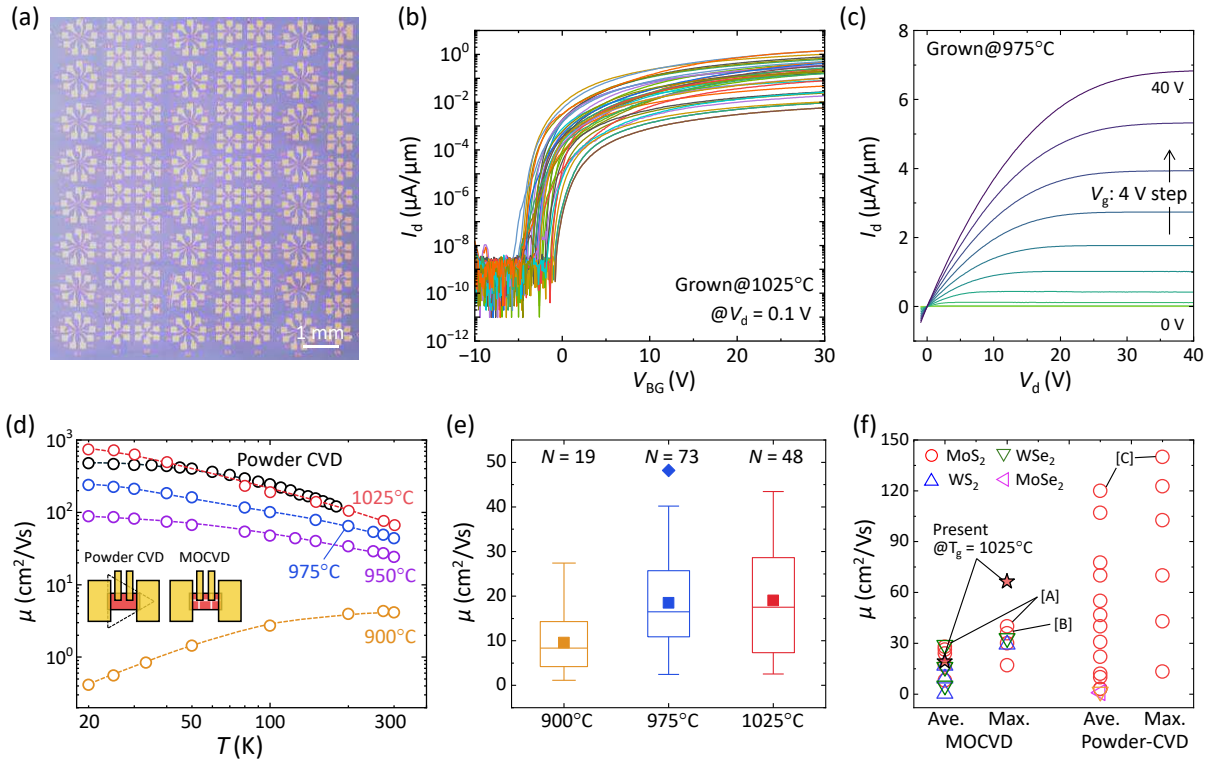

Fig. 4| Phonon limited electron mobility. a, Photograph of monolayer MoS_2 FETs on a SiO_2/Si substrate. **b**, Transfer characteristics of 48 MoS_2 FETs grown at 1025°C. **c**, Output characteristics of MoS_2 FET grown at 975°C. **d**, Temperature dependence of mobility for four-terminal MoS_2 FETs grown at various temperatures. Black circles represent reference data for powder-source CVD.[46] **e**, Statistical analysis of mobility for two-terminal MoS_2 FETs grown at various temperatures, where the Y-function method[47] was applied for evaluation. N represents the number of measured devices. **f**, Benchmark of mobility values for TMDC grown by powder CVD and MOCVD. Refs. [A], [B], and [C] are adapted from refs. 10, 43, and 48.

Methods

MOCVD growth

The MOCVD reactor employed in this study is horizontal-flow and cold-wall configuration. The graphite susceptor for single wafer is resistively heated from its backside and the maximum wafer size is 2 inches (**Supplementary Fig. S2**). Molybdenum oxychloride (MoO_2Cl_2) and hydrogen sulfide (H_2S) were utilized as the molybdenum and sulfur precursors, respectively. The MoO_2Cl_2 canister was controlled at atmospheric pressure and bath temperature of 18°C. The flow rate of N_2 passing through the canister was varied from 50 to 400 sccm to regulate the supply of MoO_2Cl_2. The H_2S flow rate was changed within the range of 2 to 20 sccm. The total N_2 flow rate in the reactor was kept at 2500 sccm. MoS_2 film was grown at substrate temperatures ranging from 800°C to 1050°C, under a constant chamber pressure of 50 Torr, with growth durations limited to a maximum of 2 hours. All the gas flow rates and pressures were controlled by mass flow controllers and automatic pressure controllers, respectively. Alternatively, precursors of $Mo(CO)_6$ and H_2S were also utilized for MOCVD growth run for comparison. The $Mo(CO)_6$ bath temperature is 5°C and the flow rate N_2 carrier gas is fixed at 20 sccm. Calculating from the sublimation pressures of MoO_2Cl_2 and $Mo(CO)_6$ described in **Supplementary Fig. S2b**, all the MoS_2 growth was conducted under sulfur-rich conditions. Sapphire substrates cutting into 2 × 2 cm^2 were usually employed for the growth experiments, while 2-inch diameter wafers were utilized for the MoS_2 growth used for device fabrication. The 2-inch c-sapphire substrates were procured by Orbray Co. Ltd. Prior to growth, thermal annealing process was performed in a muffle furnace at 1150°C in air for 1 hour to prepare surface steps aligned along the a-axis $[11\bar{2}0]$.

Characterizations

To confirm the crystal quality and thickness of films, Raman spectroscopy, PL spectroscopy and AFM were employed. Raman and PL measurements were conducted with a 532-nm excitation laser with an ~1-μm spot and ~0.5 mW. In-plane XRD measurements were performed using a Rigaku SmartLab system to identify the presence of low-angle domains in monolayer MoS_2 (**Supplementary Fig. S3**). Initially, the diffraction peak corresponding to the $\{11\bar{2}0\}$ plane of MoS_2 was observed to align with the $\{11\bar{2}0\}$ plane of the sapphire substrate, confirmed via a $2\theta\chi/\phi$ scan. Subsequently, a ϕ scan of $\{11\bar{2}0\}$ planes of MoS_2 was conducted with a typical scan rate of 0.3°/min and step width of 0.02°. Differential DF-TEM, 4D-STEM and HAADF-STEM experiments were carried out using a JEOL ARM 200F TEM with

acceleration voltages of 80, 200, and 200 kV, respectively. 4D-STEM orientation maps were generated from electron diffraction data set using a proprietary algorithm based on the NanoMEGAS ASTAR. For HAADF-STEM, the spherical aberration coefficient was less than 1 μm. The convergent angle was 17 mrad and the inner and outer angles of the ADF detector were 50 and 150 mrad, respectively. The SHG measurements were conducted using a mode-locked Ti:sapphire laser (wavelength: 810 nm, pulse width: ~100 fs, and repetition rate: 82 MHz) in a home-built optical microscope configured for backscattering (**Supplementary Fig. S10**). The LEED patterns at room temperature were acquired using a conventional LEED system (OCI, BDL600IR) under ultrahigh vacuum (UHV) conditions at 10^{-8} Pa, with a 1 eV step in the energy range from 30 to 380 eV. The LEED *I-V* curves for five non-equivalent beams were extracted from LEED patterns with the background subtracted. The total cumulative energy range covered was approximately 1455 eV.

Theoretical calculations were performed by using the PHASE/0 code,[1] which is based on DFT[2] and pseudo-potential schemes[3,4] with plane-wave basis sets. For the exchange-correlation term, the PBE form was used.[5] For the van der Waals interactions, the DFT-D2 method was applied.[6] The cut-off energies for the wavefunctions and charge density were 56 Ry and 506 Ry, respectively. The number of *k* points sampled in the Brillouin zone was more than 5×5 per the surface unit cell of c-plane sapphire. All the models were optimized to meet the force criterion of 0.02 eV/Å. Sapphire slab employed here consists of six Al_2O_3 layers and the thickness of a vacuum region is 0.9 nm. The top (bottom) layer of a sapphire slab is terminated with only one Al atom per surface unit, to make its electronic states semiconducting. The calculated lattice constant for the hexagonal MoS_2 monolayer is 0.318 nm, while that for sapphire is 0.4798 nm. In this study, the change in the lattice mismatch of MoS_2 grown on sapphire is quite essential to see the stability of MoS_2/sapphire heterostructures. Thus, the lattice constant for sapphire is set to 0.4789 nm to follow the experimental ratio of 1.506 for MoS_2 and sapphire. This treatment is justified, because there is no chemical bond between MoS_2 monolayer and sapphire slab, and the lattice constant of sapphire slab is not affected by MoS_2. Adsorption energy, Ead is defined as $E_{ad} = (E^{MoS2} + E^{sapphire} - E^{MoS2/sapphire})/S$, where E^{MoS2}, $E^{sapphire}$, and $E^{MoS2/sapphire}$ are the calculated total energies for MoS_2 monolayer, sapphire, and MoS_2/sapphire. S is the area of a superstructure.

Device fabrication and transport characterization

To evaluate the transport properties of monolayer MoS_2 grown by MOCVD, it was transferred onto a 90-nm SiO_2/n^+-Si substrate using a standard transfer technique (**Supplementary Fig. S18**). Polymethyl methacrylate (PMMA, MicroChem, 495k) was spin-coated on the MoS_2/sapphire wafer and further supported by thermal release tape (TRT, Nitto, Revalpha). The TRT/PMMA/MoS_2 stack was released from the sapphire wafer in a KOH solution (1 mol/L) and rinsed with deionized water. Following this, the stack was transferred to the SiO_2/Si substates, and the TRT/PMMA film was removed in acetone. For device fabrication, a maskless aligner μMLA (Heidelberg instrument) with double layer resists (PMGI SF5/AZ1500) and NMD-3 developer was used to define channel and electrode patterns. Then, the shape of MoS_2 channels were defined by CF_4 plasma etching. A 1-nm/30-nm Ni/Au electrode was deposited in an UHV chamber at a base pressure of ~5×10^{-8} Pa with a low deposition rate of 0.0014 Å/s for Ni and 0.15 Å/s for Au. The sample temperature was maintained at 15°C in the UHV chamber to avoid thermal damage. All electrical measurements in this study were conducted using a vacuum prober with a cryogenic system, employing a Keysight B1500 semiconductor parameter analyzer.

Data availability

The data that support the findings of this study are available from the corresponding authors upon reasonable request.

References

1. Yamasaki, T. *et al.* Multi-axis decomposition of density functional program for strong scaling up to 82,944 nodes on the K computer: Compactly folded 3D-FFT communicators in the 6D torus network. *Comput Phys Commun* **244**, 264–276 (2019).
2. Kohn, W. & Sham, L. J. Self-consistent equations including exchange and correlation effects. *Physical Review* **140**, A1133–A1138 (1965).
3. Troullier, N. & Martins, J. L. Efficient pseudopotentials for plane-wave calculations. *Phys Rev B* **43**, 1993–2006 (1991).
4. Vanderbilt, D. Soft self-consistent pseudopotentials in a generalized eigenvalue formalism. *Phys Rev B* **41**, 7892–7895 (1990).
5. Perdew, J. P., Burke, K. & Ernzerhof, M. Generalized gradient approximation made simple. *Phys Rev Lett* **77**, 3865–3868 (1996).
6. Grimme, S. Semiempirical GGA-type density functional constructed with a long-range dispersion correction. *J Comput Chem* **27**, 1787–1799 (2006).

Acknowledgements

Theoretical calculations were performed by using the Numerical Materials Simulator of NIMS and the Earth Simulator (ES) of JAMSTEC. This research was supported by the JSPS KAKENHI (Grant Numbers: JP17H03241, JP21H05237, JP21H05232, JP22H04957, JP22K04212, JP23K13622, JP23K03272, and JP23K04592), Iketani Science and Technology Foundation, the NICT (Grant Number: 05901), the JST-Mirai Program (Grant Number: JPMJMI22708192) and JST-CREST (Grant Number: JPMJCR24A3).

Author contributions

Y.S., Y.O., and T.M. contributed to the MOCVD growth, as well as AFM and Raman spectroscopy measurements. S.L. performed PL measurements. T.H. conducted XRD measurements, while A.O. performed LEED analysis. J.N. carried out DFT simulations. E.K., T.Y., X.Y., and N.I. performed HAADF-STEM measurements. A.S., and M.I. conducted SHG measurements. K.A. fabricated the devices and conducted electrical characterization with assistance from K.K. and T.N. All authors contributed to the discussion, and K.N. and Y.S. co-wrote the manuscript with input from all authors.

Competing interests

The authors declare no competing interests.

Additional information

Supplementary information

The online version contains supplementary material available at.

Supplementary information

Self-aligned and self-limiting van der Waals epitaxy of monolayer MoS_2 to annihilate grain boundaries for scalable 2D electronics

Yoshiki Sakuma[1*], Keisuke Atsumi[2], Takanobu Hiroto[3], Jun Nara[4], Akihiro Ohtake[1], Yuki Ono[5], Takashi Matsumoto[5], Emi Kano[6], Toshiki Yasuno[6], Xu Yang[6], Nobuyuki Ikarashi[6], Asato Suzuki[7], Michio Ikezawa[7], Shuhong Li[2], Tomonori Nishimura[2], Kaito Kanahashi[2], Kosuke Nagashio[2*]

[1]Research Center for Electronic and Optical Materials, National Institute for Materials Science, 1-1 Namiki, Tsukuba 305-0044, JAPAN
[2]Department of Materials Engineering, The University of Tokyo, 7-3-1 Hongo, Bunkyo-ku, Tokyo 113-8656, Japan
[3]Research Network and Facility Services Division, National Institute for Materials Science, 1-2-1 Sengen, Tsukuba 305-0047, Japan
[4]Research Center for Materials Nanoarchitectonics, National Institute for Materials Science, 1-1 Namiki, Tsukuba 305-0044, JAPAN
[5]Tokyo Electron Technology Solutions Limited, 650 Mitsuzawa, Hosaka-cho, Nirasaki, 407-0192, Japan
[6]Institute of Materials and Systems for Sustainability, Nagoya University, Furo-cho, Chikusa-ku, Nagoya, 464-8601, Japan
[7]Department of Physics, University of Tsukuba, 1-1-1 Tennodai, Tsukuba, 305-8571, Japan

*sakuma.yoshiki@nims.go.jp, *nagashio@material.t.u-tokyo.ac.jp

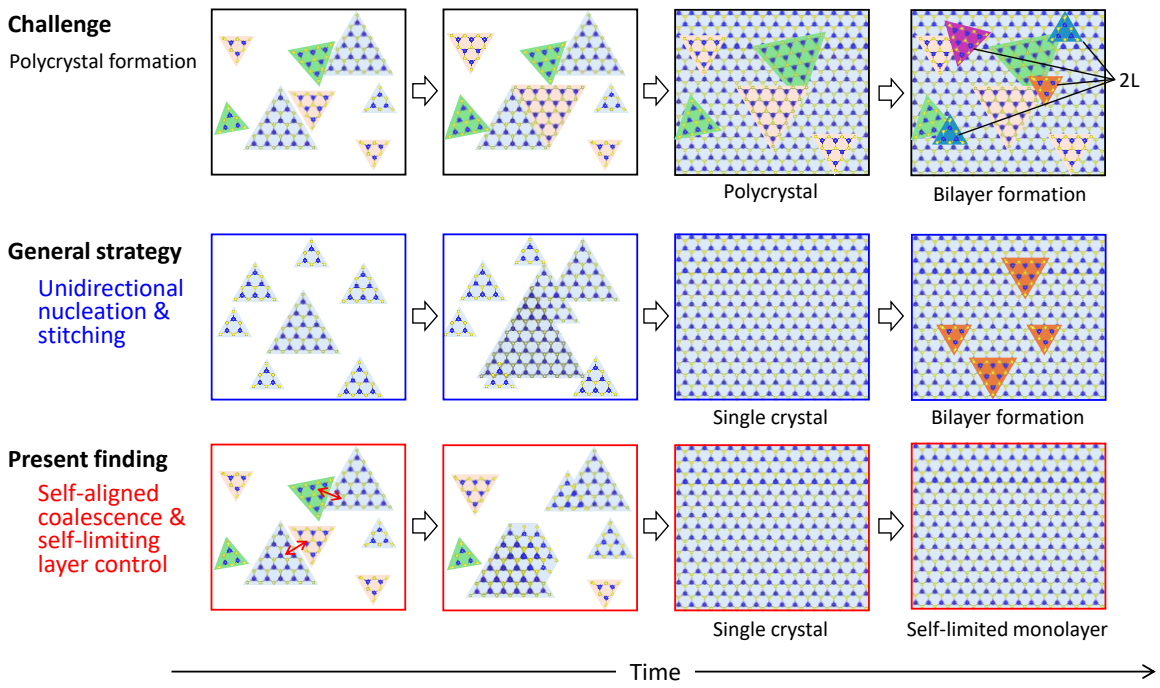

Figure S1 Schematic illustration showing the challenge for wafer-scale epitaxial growth and two kinds of growth strategies for single crystal formation.

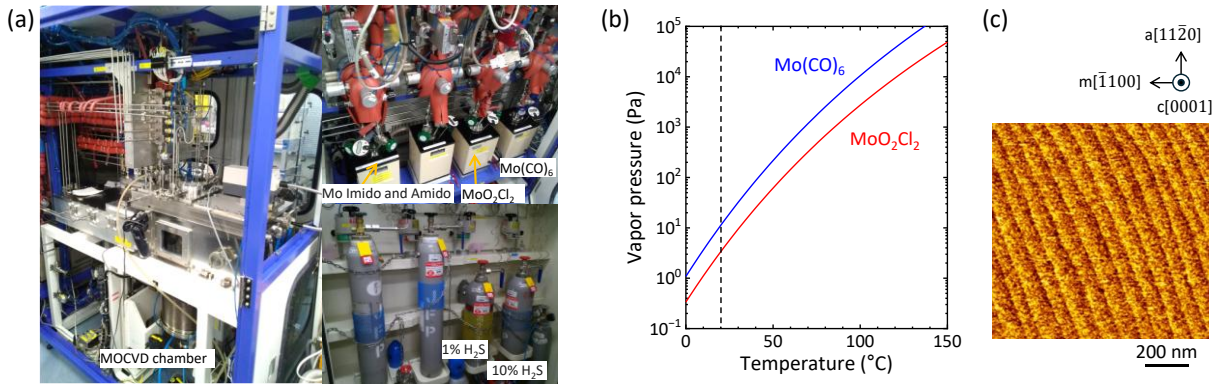

Figure S2 (a) Photograph of a horizontal cold-wall MOCVD reactor with the carbon-free MoO_2Cl_2 and H_2S gas sources. Although, MoO_2Cl_2 is classified into inorganics to be precise, not organometals, this precursor can be used with the same way in conventional MOCVD growth system. Therefore, for simplicity, we call our synthetic method MOCVD in this report. (b) Vapor pressures of MoO_2Cl_2 and $Mo(CO)_6$ as a function of temperature. (c) AFM image of pretreated sapphire surface with step and terrace structure.

Note: Thermal stability, in particular, disproportionate decomposition, and volatility of several kinds of molybdenum oxychlorides are described in the literatures.[1,2] MoO_2Cl_2 is the most stable and has higher sublimation pressure among them.[3] According to Saeki et al., the sublimation pressure is given by equation (1) at the temperature range of 50-157°C.[2] In contrast, Ohta et al. reported the sublimation from solid $Mo(CO)_6$ as equation (2) at the range of -10.5-23.1°C.[4] In (b), to compare the sublimation property between two precursors, we plotted the pressures by extrapolating the temperature range to 0°C-150°C.

$$\mathrm{Log_{10}}\ P\ (\mathrm{mmHg}) = -3830/T\ (\mathrm{K}) + 11.747 \qquad (1)$$

$$\mathrm{Log_{10}}\ P(\mathrm{Pa}) = 14.9 - 4058/T(\mathrm{K}) \qquad (2)$$

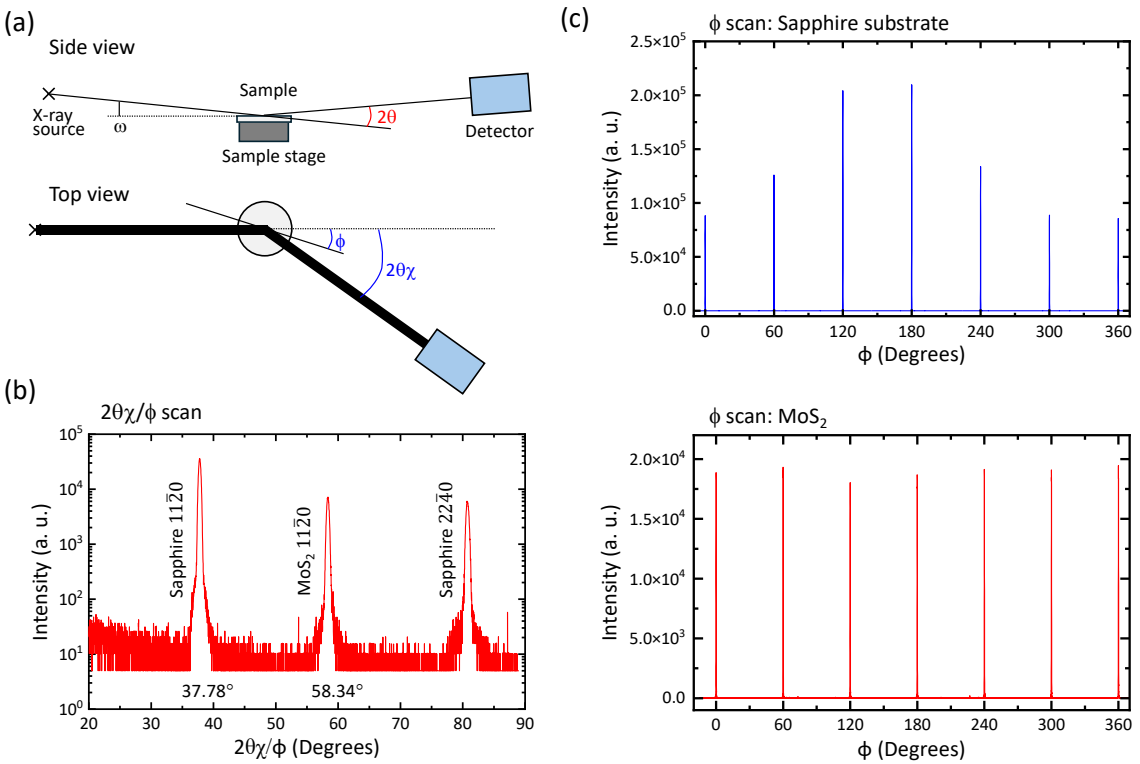

Figure S3 (a) In-plane XRD measurement setup for 2θχ/ϕ scan and ϕ scan. Top view shows the situation where reflection from targeted {11$\bar{2}$0} plane is measured. (b) 2θχ/ϕ scan for MoS_2 on the sapphire substrate. (c) In-plane XRD azimuthal angle (ϕ) scans of {11$\bar{2}$0} planes for sapphire substrate (α-Al_2O_3) and monolayer MoS_2, respectively.

Note: The basic procedures to make in-plane XRD measurements using Rigaku SmartLab diffractometer was described in the **Method** section.[5] As shown in (b), the diffraction peak corresponding to the {11$\bar{2}$0} plane of MoS_2 was observed to be parallel to that of the sapphire substrate, i.e., [11$\bar{2}$0]MoS_2//[11$\bar{2}$0]α-Al_2O_3. At fixed 2θχ angles of 37.78° and 58.34°, azimuthal ϕ scans of {11$\bar{2}$0} planes in both sapphire substrate and MoS_2 were conducted separately. The ϕ scan was conducted over 0°-360° under faster scan rate of 20°/min as shown in this figure. In some cases, however, the ϕ range was narrowed to 0°-180° for a high-precision slow scan of 0.3°/min to shorten the measurement time. The peak resolution of the in-plane ϕ-scan is approximately ~0.2°, which was confirmed by the sapphire 11$\bar{2}$0 substrate peak. As clearly seen in (c), the strong diffraction peaks reflected from the {11$\bar{2}$0} planes of MoS_2 appeared with 60° intervals. This indicates that monolayer MoS_2 film contains negligible twisted MoS_2 domains and shows a high-quality in-plane epitaxial alignment with sapphire substrate. It should be noted that the origin of the ϕ coordinates shown in (c) were intentionally shifted, for clarity, from the absolute values obtained by 2θχ/ϕ scans for MoS_2 and sapphire, with considering the offset angle of ϕ between MoS_2 and sapphire of 10.28° = (58.34°-37.78°)/2.

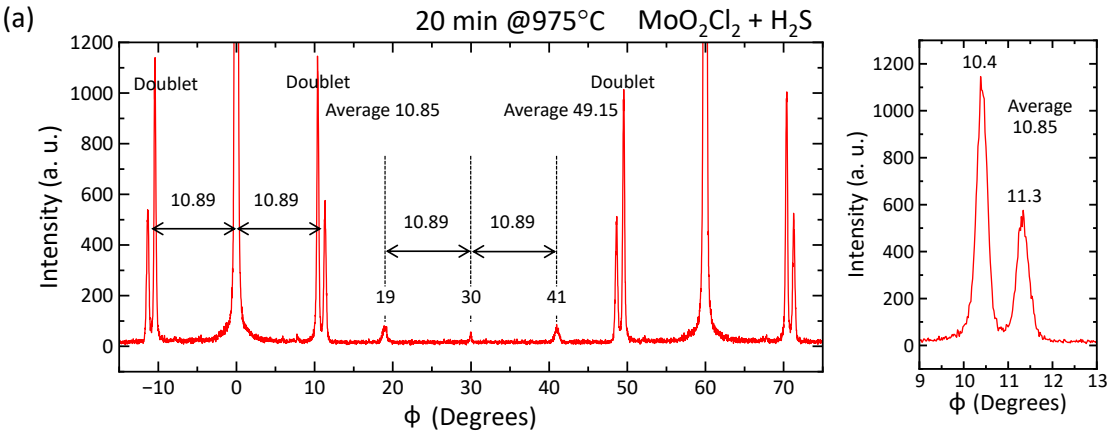

(b)

Sapphire (4.759 Å)		MoS_2 (3.161 Å)		Super cell	
Notation	Cell size (Å)	Notation	Cell size (Å)	Mismatch (%)	Twist angle (°)
$\sqrt{3} \times \sqrt{3}$ R30°	8.24	$\sqrt{7} \times \sqrt{7}$ R19.11°	8.36	+1.461	10.89
2×2 R0°	9.52	3×3 R0°	9.48	-0.368	0
$\sqrt{7} \times \sqrt{7}$ R19.11°	12.59	4×4 R0°	12.64	+0.420	19.11 (=30-10.89)
3×3 R0°	14.28	$\sqrt{19} \times \sqrt{19}$ R23.41°	13.78	-3.492	23.41
3×3 R0°	14.28	$\sqrt{21} \times \sqrt{21}$ R10.89°	14.49	+1.461	10.89
$2\sqrt{3} \times 2\sqrt{3}$ R30°	16.49	5×5 R0°	15.81	-4.129	30
$2\sqrt{3} \times 2\sqrt{3}$ R30°	16.49	$3\sqrt{3} \times 3\sqrt{3}$ R30°	16.43	-0.368	0
$2\sqrt{3} \times 2\sqrt{3}$ R30°	16.49	$2\sqrt{7} \times 2\sqrt{7}$ R19.11°	16.73	+1.461	10.89
$\sqrt{13} \times \sqrt{13}$ R13.9°	17.16	$3\sqrt{3} \times 3\sqrt{3}$ R30°	16.43	-4.276	16.10

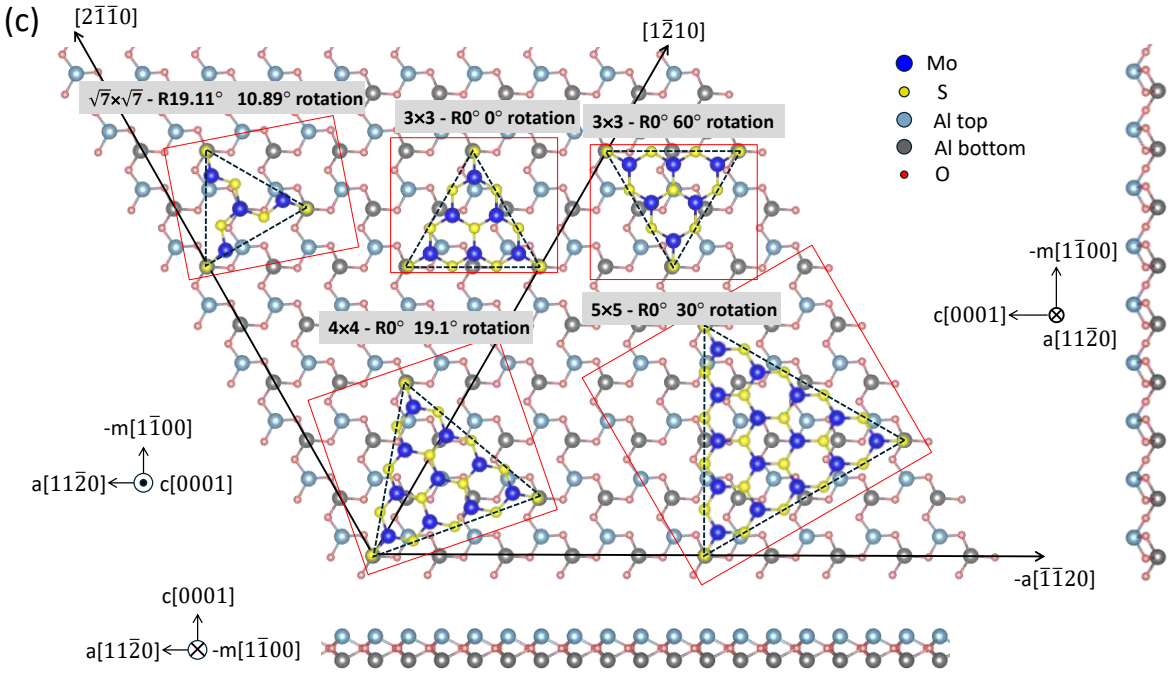

Figure S4 (a) In-plane XRD azimuthal angle (ϕ) scans of $\{11\bar{2}0\}$ planes for MoS_2 grown at 975°C for 20 min with a step width of 0.02° and a scan rate of 0.3°/min. In the right figure, the peaks around 10.85° were magnified. The observed azimuthal angles indicate the relative in-plane twisted angles between the $(11\bar{2}0)$ plane of MoS_2 and the $(11\bar{2}0)$ plane of c-plane sapphire. (b) Supercell relations of the MoS_2 and sapphire substrate.[6] For simplicity, nine pairs with a twisted angles between 0° and 30° as well as a lattice mismatch of less than 5% have

been listed. The domains with twisted angles shown in red were experimentally confirmed. (c) Schematic illustrations for MoS_2 domains with 4 sets of supercell relations which was experimentally observed in (a), plus 60° antiparallel domain. To highlight the three-fold symmetry of the sapphire substrate with single-layer Al top surface, top and bottom Al atoms were colored differently, as shown in the side view of right figure. It should be noted that (c) presents only several representative examples and does not include all the allowed atomic models. Notably, the mirror image domains with respect to a-axis and m-axis are not shown here, other than the 60° antiparallel domain. Furthermore, we have not considered the exact overlaid structures of MoS_2 domains with the sapphire surface. Determining the most energetically stable configuration for each domain is beyond the scope of this paper.

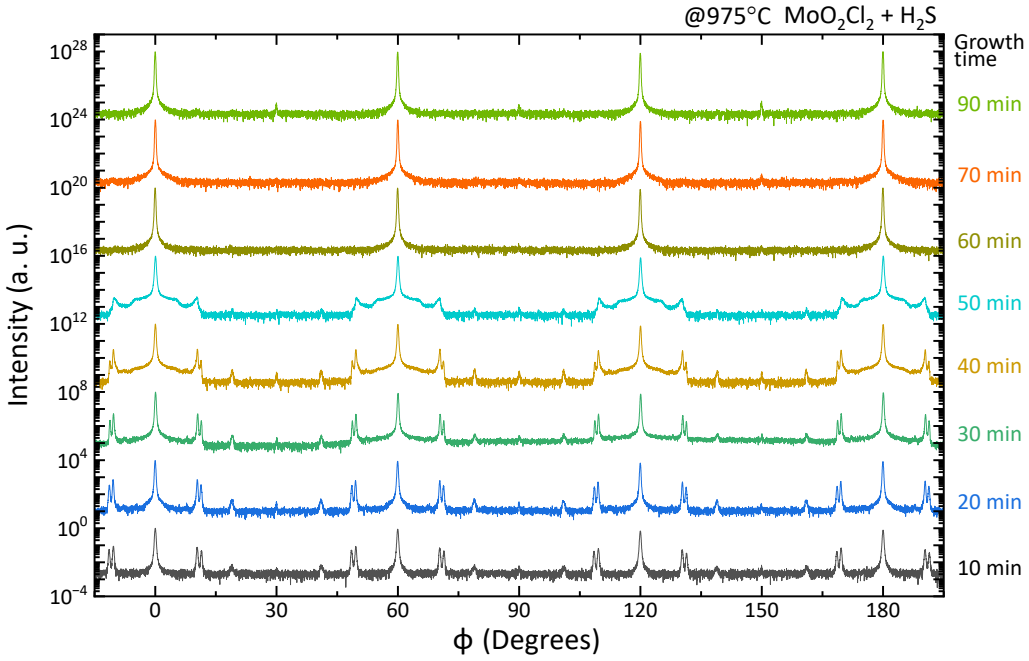

Figure S5 In-plane XRD azimuthal angle (ϕ) scans of $\{11\bar{2}0\}$ planes for MoS_2 grown at 975°C for various growth durations, ranging from 10 min to 90 min.

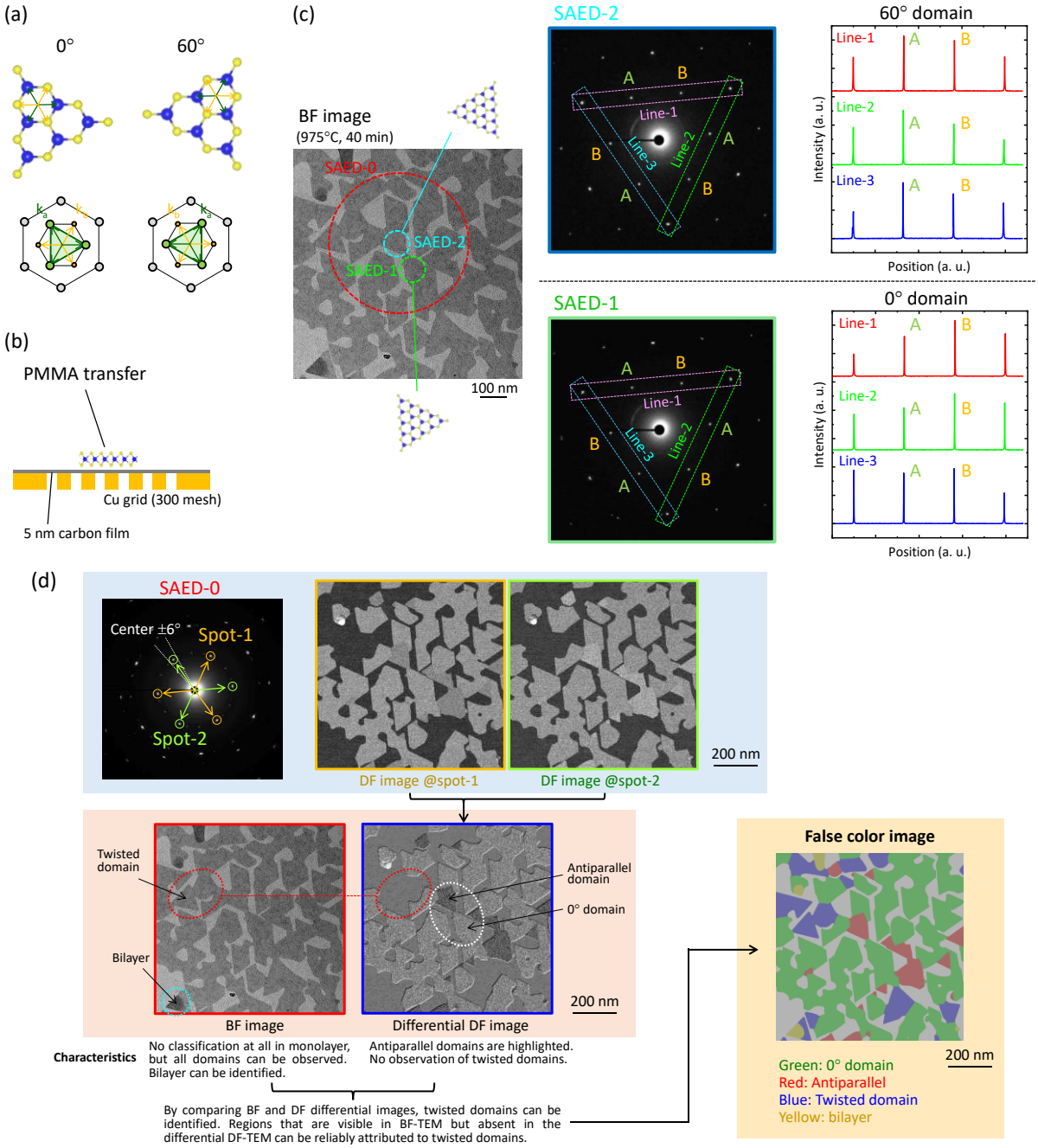

Figure S6 (a) Atomic configurations of 0° and 60° triangular domains with sulfur zigzag edges (S_{zz}) in monolayer MoS_2 and their corresponding electron diffraction patterns. Theoretically, the diffraction spot intensities associated with the reciprocal lattice vectors k_a are consistently more pronounced than those corresponding to k_b due to the violation of Friedel's law.[7] (b) Schematic representation of the sample preparation procedure employed for differential DF-TEM analysis. Monolayer MoS_2 was transferred from a sapphire substrate to a TEM grid with 5-nm amorphous carbon film via the PMMA-assisted wet transfer method. (c) Schematic illustration of the methodology for distinguishing 0° and 60° antiparallel domains based on the violation of Friedel's law. MoS_2 sample grown at 975°C for 40 min was selected as an example. Following the acquisition of a BF-TEM image, selected-area electron diffraction (SAED)

patterns were recorded at two positions, denoted SAED-1 and SAED-2. Electron diffraction intensities were subsequently obtained along three lines (line-1 to line-3). It is evident that the intensities at spots B(A) are always higher than A(B) at SAED-1(2), confirming the violation of Freidel law. It should be noted that, by considering the shape of triangular domains in BF-image, this relationship is the opposite to the theoretical prediction shown in (a). This might be an issue arising from the optical system in TEM, such as the camera settings. Therefore, we carried out these experiments while checking the relationship between the direction of three triangles in the employed TEM system: 1) the triangular pattern formed by connecting the bright diffraction spots (A or B), 2) the geometric direction of the triangular region in DF-image, and 3) the triangle of the Mo sublattice (requiring observations by atomic resolution HAADF-STEM). Consequently, it is also verified that the triangular domains have S_{zz} edges as illustrated in (a) in our typical growth conditions. (d) Schematic illustration of the differential DF-TEM strategy employed to construct false-color domain maps. Initially, SAED was acquired over a relatively wide area (SAED-0 in (c)). Since 0° and 60° antiparallel domains are always dominant at any area on the sample, spot-1 and spot-2 with the relation of 180° inversion can be selected, thereby violating Friedel's law. Therefore, two sets of DF-TEM images were acquired at diffraction spots 1 and 2 using a minimal objective aperture (±6°). In the differential DF-TEM image, 0° and 60° antiparallel domains are clearly distinguished because the contrast is doubly emphasized. Note that only domains with twist angles within ±6° are identified as 0°/60° domains due to the finite mechanical aperture size in this method. Conversely, domains where the diffraction spot is outside the objective aperture are not observed in the dark-field image, which can be judged as rotating domains. Subsequently, a BF-TEM image was obtained, where all domains are visible. By comparing the differential DF-TEM image with the BF-TEM image, the regions where no domains are observed in differential DF-TEM but are visible in BF-TEM can be recognized as twisted domains. Finally, this approach enables the construction of a comprehensive false-color domain map for monolayer MoS_2.

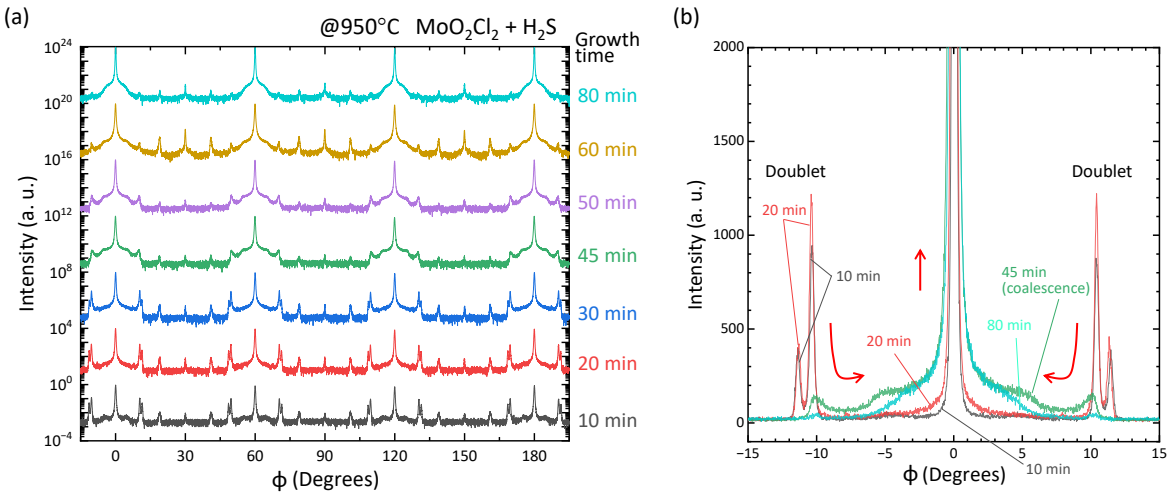

Figure S7 In-plane XRD azimuthal angle (ϕ) scans of $\{11\bar{2}0\}$ planes for MoS_2 grown at 950°C for various growth durations, ranging from 10 min to 80 min. (a) Full scan range data and (b) superimposed data focusing on the 0° domains with the doublet subpeaks at 10.4° and 11.3°.

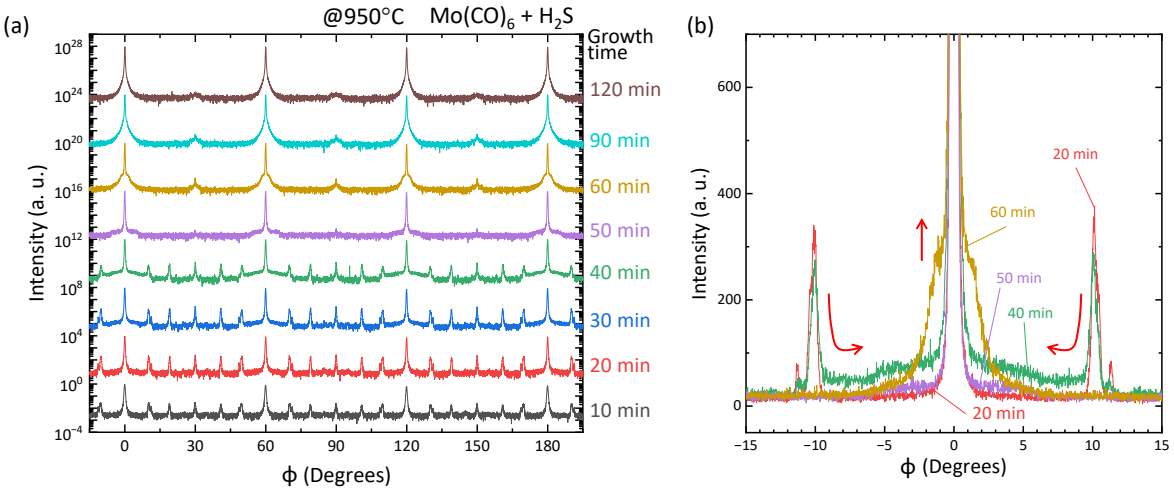

Figure S8 In-plane XRD azimuthal angle (ϕ) scans of $\{11\bar{2}0\}$ planes for MoS_2 grown at 950°C for various growth durations, ranging from 10 min to 120 min. The precursors used in this experiment are $Mo(CO)_6$ and H_2S, which are common in previous literature. (a) Full scan range data and (b) superimposed data focusing on the 0° domains with the doublet subpeaks at 10.4° and 11.3°. These results imply that the formation of single crystals via self-aligned coalescence is not exclusive to the MoO_2Cl_2 precursor employed in this study.

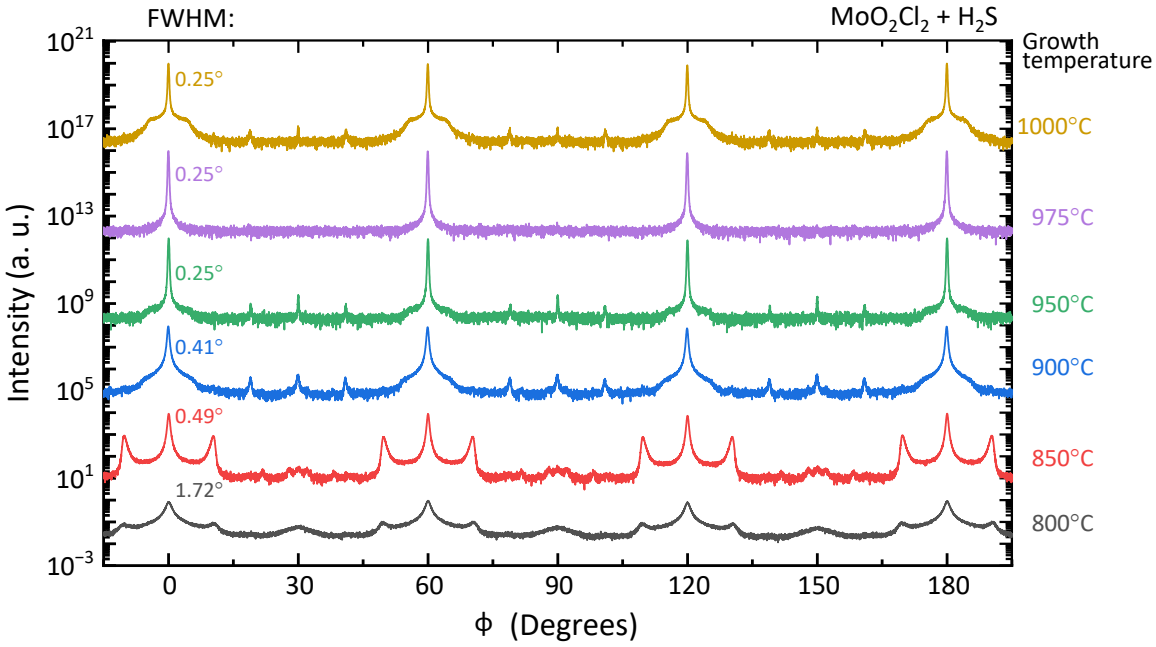

Figure S9 In-plane XRD azimuthal angle (ϕ) scans of $\{11\bar{2}0\}$ planes for MoS_2 grown for 60 min at various growth temperatures, ranging from 800°C to 1000°C. It should be noted that below 900°C, the main peak intensity decreases, and the half-width broadens, indicating the degradation of crystallinity and increased in-plane mosaicity. Notably, at 850°C and 800°C, the peak originating from the 11° rotated domain remains even after full coverage, suggesting that the self-aligned coalescence does not proceed efficiently.

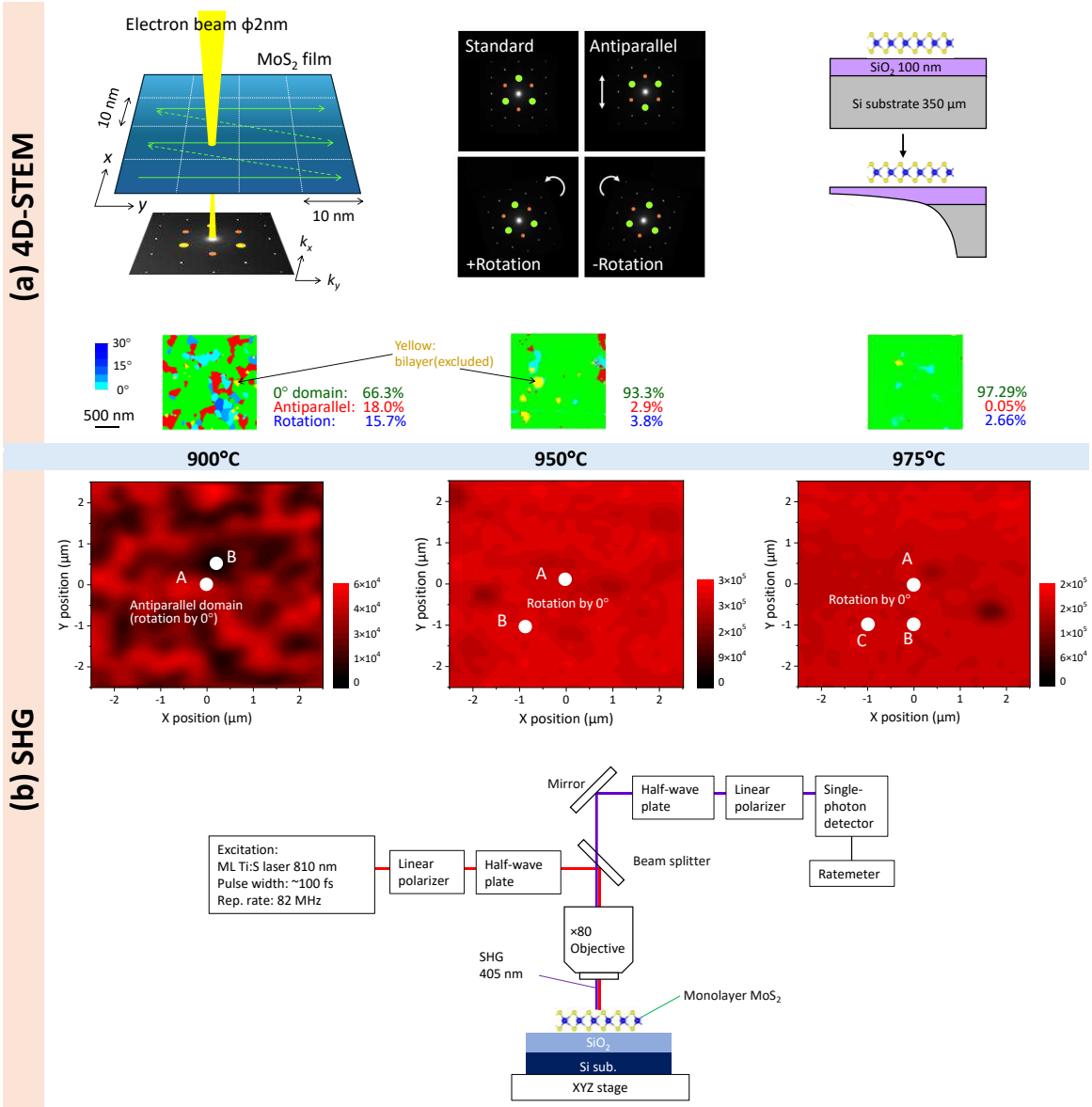

Figure S10 Comparison between 4D-STEM and SHG results. (a) Four distinct types of diffraction patterns -standard (0°), antiparallel (60°), clockwise rotation, and anticlockwise rotation- can be identified through 4D-STEM measurements. 4D-STEM mappings for MoS_2 obtained at various growth temperatures. Schematic of the sample preparation for differential DF-TEM analysis is also shown. Monolayer MoS_2 was transferred from a sapphire substrate to a SiO_2/Si substrate using the PMMA wet transfer method. Subsequently, the backside Si was etched by ion milling, reducing the SiO_2 thickness much less than 50 nm to avoid electron scattering effect. (b) Schematic representation of the optical setup used for SHG measurements and SHG mapping images for MoS_2, obtained at various growth temperatures.

Note: (4D-STEM) The 4D-STEM technique[8,9] enables the rapid acquisition of 2-nmϕ nanobeam electron diffraction patterns over a 2D array of spatial positions with a 10-nm pitch. Computational analysis of this dataset reveals structural variations on a pixel-by-pixel basis.

For a fully continuous monolayer MoS_2 film grown at 900°C for 60 min, the 0° domains, represented in green, are dominant, while low-angle domains (blue) and antiparallel domains at 60° (red) coexist. Additionally, the yellow regions represent the bilayer, which is not included in the overall ratio calculation.

Note (SHG) Schematic representation of the optical setup used for SHG measurements. Excitation light from a Ti:sapphire laser (wavelength: 810 nm, pulse width: ~100 fs, repetition rate: 82 MHz, intensity: 1 mW) was passed through a linear polarizer and a half-wave plate to control the polarization plane. The light was focused onto the sample surface using an 80× objective lens. The generated SHG signal was collected through the same objective lens, passed through a detection half-wave plate and a linear polarizer, and then directed to a photodetector. Two sets of half-wave plates were adjusted to ensure parallel polarization conditions. For polarization-resolved SHG measurements, these half-wave plates were systematically rotated to analyze the polarization dependence under parallel conditions.

SHG mapping images for MoS_2, obtained at various growth temperatures, were recorded at the polarization angle corresponding to the armchair direction. For the 850°C sample (not shown here), where the armchair direction varies across domains, the polarization angle was set based on the armchair direction determined at a representative point. It should be noted that the maximum SHG intensities differ across all images. At 900°C, positions A and B showed no rotational difference but demonstrated a notable intensity disparity, suggesting the presence of antiparallel domains. Although SHG is insensitive to antiparallel domains due to the six-fold pattern, the intensity is substantially suppressed at mirror twin boundary as well as tilted GBs.[10] At temperatures exceeding 950°C, the absence of rotational differences and the uniform intensity levels indicate that all domains are well-aligned, which agrees well with the 4D-STEM results.

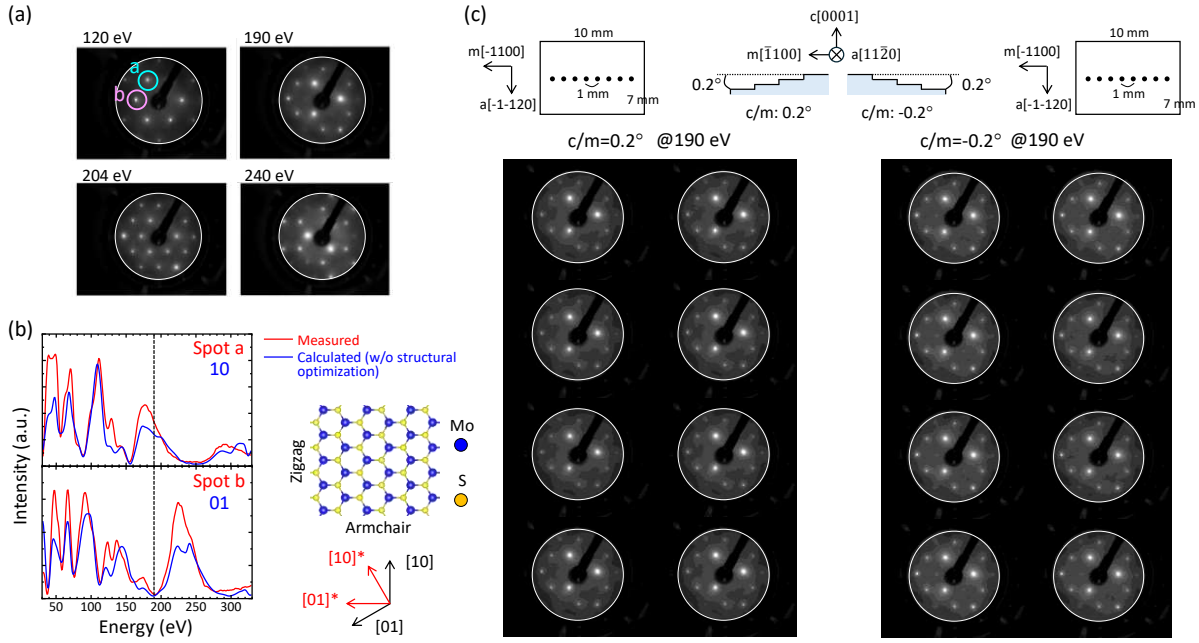

Figure S11 (a) Representative LEED patterns of monolayer MoS_2 acquired at various electron energies for the miscut angle of c/m = -0.2°. Monolayer MoS_2 was grown on sapphire substate at 975°C. (b) Experimentally obtained LEED *I-V* curves (red) for diffraction spots of "a" and "b" in (a) with simulated curves (blue) for diffraction spots of 10 and 01. (c) Schematic illustration of a monolayer MoS_2 film on a sapphire substrate where eight measurement points for LEED analysis are indicated. Two types of sapphire substrates with miscut angles of c/m = 0.2° and -0.2° were prepared for comparison. Eight LEED patterns are shown for each substrate.

Note: Initially, LEED patterns of monolayer MoS_2 grown on sapphire substrates with a standard miscut angle of c/m = -0.2° were acquired at various electron beam energies, as shown in (a). Two representative diffraction spots, "a" and "b", were selected to assess the possible presence of antiparallel domains. Then, LEED *I-V* spectra (the intensity variations of diffraction spots as a function of the electron energy) for these spots were measured (red curves), as shown in (b). To determine the crystallographic origin of each diffraction spot, LEED *I-V* curves for the 10 and 01 spots of a monolayer MoS_2 single crystal, based on the atomic structure illustrated schematically, were computed using the SATLEED package developed by Barbieri and Van Hove. [11–13] As clearly seen in (b), the experimental LEED *I-V* curves for spots "a" and "b" closely match the simulated curves for the 10 and 01 spots, respectively. This agreement confirms that the monolayer MoS_2 is a single crystal and contains no antiparallel domains. To assess the single crystallinity of MoS_2 across the wafer, LEED patterns at 190 eV with a threefold symmetry were measured at eight locations across the sample. All locations exhibited identical threefold symmetric diffraction patterns, even on samples with an opposite miscut angle of c/m = 0.2°. Moreover, monolayer MoS_2 grown on a sapphire substrate with a different

miscut angle of c/a = +0.15° displayed LEED *I-V* curves that remained consistent with the others. These results strongly indicate that the orientation of monolayer MoS_2 film is uniformly aligned across the wafer and that the epitaxial alignment during MOCVD growth is dictated not by step-edge directionality but by the interaction between MoS_2 and the underlying sapphire surface structure.

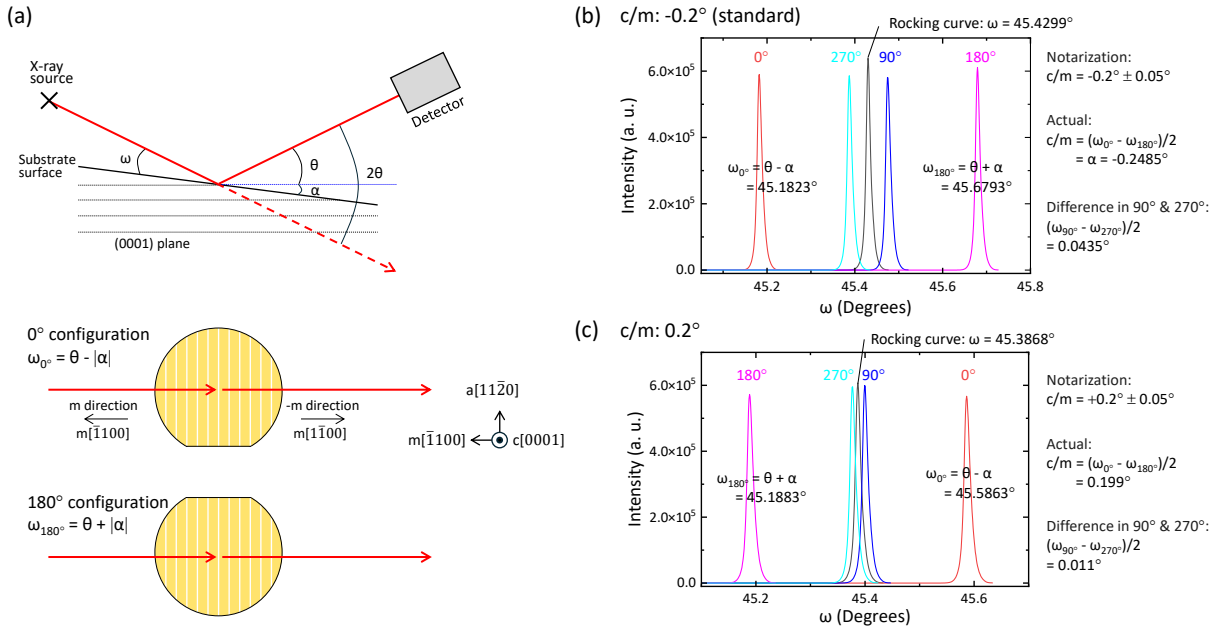

Figure S12 (a) Out-of-plane XRD measurement setup for determining the miscut angle toward -m direction (c/m = -|α|°) of standard sapphire substrate. Wafer setting configurations for 0° and 180° setups. XRD rocking curve measurements of (b) c/m = -0.2° and (c) c/m = +0.2°.

Note: The miscut angle of the sapphire substrate was evaluated by rocking curve measurements[14] using Rigaku SmartLab diffractometer equipped with a Ge (220) two-bounce channel-cut monochromator and HyPix-3000 detector. Initially, the sapphire substrate, oriented with a miscut angle of c/m = -0.2° (standard), was mounted on sample stage with the 0° configuration as depicted in (a), while the detector was positioned at the 2θ angle of 90.8° to match with the 00012 diffraction angle. Subsequently, the ω axis underwent rotation, leading to the peak intensity at $\omega_{0^\circ} = \theta - |\alpha| = 45.1823^\circ$, as illustrated in (b). Following this, the sapphire substrate was 180° rotated in plane (referred to as the 180° configuration), and the peak was found at $\omega_{180^\circ} = \theta + |\alpha| = 45.6793^\circ$ in the same way. Consequently, the miscut angle -|α| was determined to be $(\omega_{0^\circ} - \omega_{180^\circ})/2 = -0.2485^\circ$, a value within the expected range considering the specified tolerance of -0.2° ± 0.05°. Measurements were also conducted at the 90° and 270° configurations. The incidental miscut angle along the a-axis was found to be negligible, assessed at 0.0435°. Furthermore, the miscut angle +|α| for the sapphire substrate with c/m = +0.2° was similarly evaluated to be +0.199°, as depicted in (c).

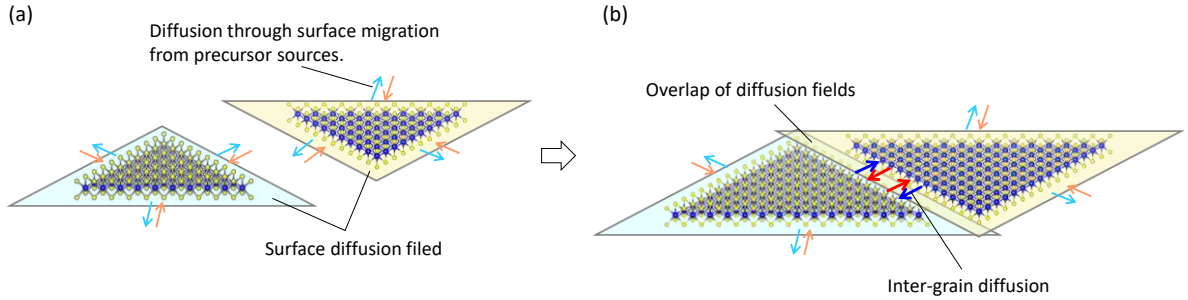

Figure 13 Schematic illustration of atomic diffusion between adjacent grains with overlapping diffusion fields.

Note: Although studies on the atomistic mechanisms of GB motion in TMDCs remain limited, the dynamics of inversion domain annihilation have been reported in relation to the GB migration.[15] GB migration could play a pivotal role in driving the self-aligned coalescence of misoriented domains into a 0° domain on the sapphire substrate, thereby facilitating GB annihilation. Meanwhile, it is considered that Mo- and S-containing species or elements frequently attach to and detach from the growing grain edges during MOCVD, generating surface diffusion fields around the grain peripheries. These diffusion fields can overlap prior to physical impingement, enabling mass transport between grains, as shown in (b), which is generally observed in the Ostwald ripening process.

In the MOCVD growth, the selection of precursors significantly affects the surface diffusivity of growth species. Nonetheless, time-resolved in-plane XRD measurements using two distinct Mo precursors, MoO_2Cl_2 (**Figure 1c** and **Supplementary Fig. S5**) and $Mo(CO)_6$ (**Supplementary Fig. S8**), revealed no substantial differences in the self-aligned coalescence behavior, implying that surface diffusion may not critically impact GB migration. However, it remains premature to definitively exclude its potential contribution, given the absence of conclusive evidence. Indeed, **Figure 1d** and **Supplementary Fig. S6** involve the important results that suggest the existence of surface diffusion. They reveal that initially isolated, triangular domains undergo morphological evolution during coalescence, with sharp convex and concave edge intersections changing into rounded shapes. This behavior is apparently indicative of curvature-driven mass transport via surface diffusion on the sapphire substrate.

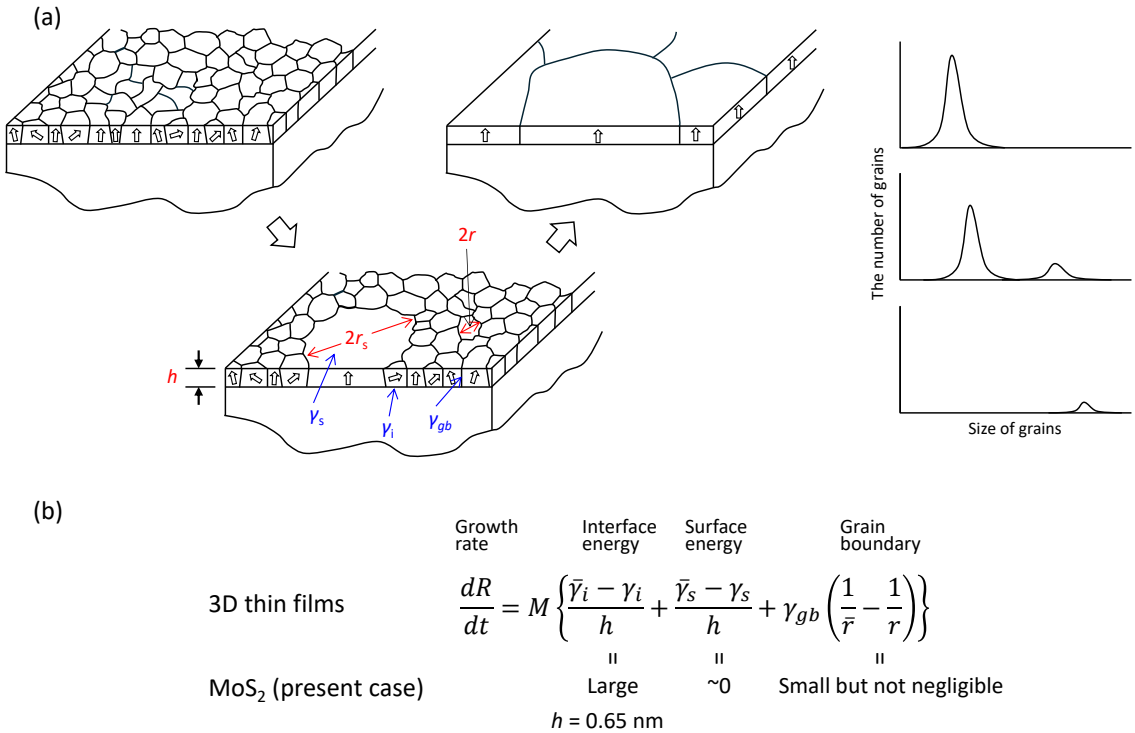

Figure S14 (a) Schematic representations of epitaxial grain growth (EGG) in polycrystalline thin films on single crystalline substrates for conventional metallic systems,[16,17] Secondary grain growth is observed in the absence of nucleation of new grains. (b) The rate of grain growth is presented, where M denotes the average grain boundary mobility, γ_{gb} represents the average grain boundary energy, $\bar{r}$ is the average grain radius, r is the radius of the grain under consideration, r_s is the radius of the secondary grain, h is the film thickness, which is smaller than grain size. Additionally, γ_s is the surface energy of the growing grain, γ_i is the energy at the grain/substrate interface, $\bar{\gamma}_i$ and $\bar{\gamma}_s$ are the average values for the entire film.

Note: For the metallic 3D thin film system, both $\bar{\gamma}_i$ and $\bar{\gamma}_s$ exhibit a strong dependence on the crystallographic orientation of individual grain. Grains with orientations that minimize the total energy (including both surface and interface contributions) preferentially grow more rapidly than grains with other orientations, provided that the initial grain sizes are approximately equivalent. Consequently, grain growth driven by surface and interface energies in films on single crystal substrates results in three-dimensionally constrained, epitaxial orientations, i.e., epitaxial grain growth is anticipated.

In contrast, additional intrinsic characteristics must be considered for 2D materials such as MoS_2. Owing to the absence of dangling bonds, the surface energy of MoS_2 is effectively negligible. Furthermore, since the film thickness, h, is limited to merely 0.65 nm, it is reasonable to assume that the interfacial energy term becomes crucial as the main driving force for single crystal formation in high-temperature MOCVD. This idea explains why the low angle rotated domains converge to the 0° domain. However, as predicted by DFT calculations (**Figure**

2e and **Supplementary Fig. S15b**), there may not be a significant difference in the interfacial energy between the 0° and 60° domains on sapphire. The disappearance of the antiparallel domains seems to require consideration of another factor, namely the GB energy in the third term on the right side of the above equation. It is reported that the formation of GBs is accompanied by localized strain accumulation near the boundaries in monolayer MoS_2.[15,18,19] This strain serves as the driving force contributing to grain boundary annihilation for minimizing the total energy of system.

In fact, as seen in the 45 min sample shown in **Figure 1d**, the remaining low angle and antiparallel domains are already surrounded by the 0° domains and their size are small. Therefore, even if the interfacial energies of the 0° and 60° domains are almost the same, it is quite possible that curvature-driven GB migration occurs due to energy gain, by reducing the GB length and eventually disappearing. Thus, although the dominant driving force for single-crystal formation would be the interface energy term, the GB energy term may also play an important role, particularly in the annihilation of antiparallel and low-angle domains that persist just prior to achieving complete monolayer coverage.

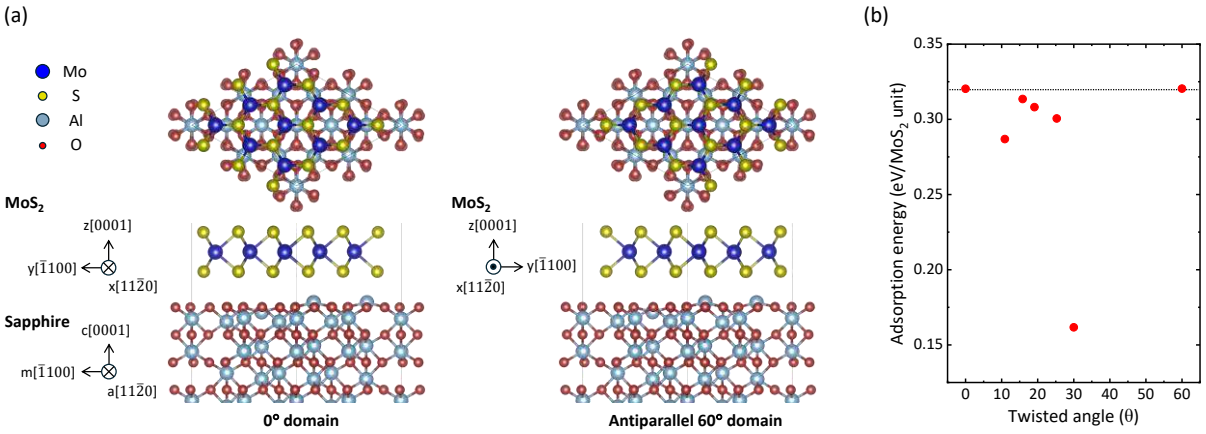

Figure S15 (a) Schematic illustration of the 0° and antiparallel 60° domain monolayer MoS_2 on the sapphire substrate. Sapphire substrate with semiconductor property was structurally stabilized with monolayer MoS_2, where the rearrangement of top Al atoms can be seen. Note that the orientation of the 0° domain monolayer MoS_2 on the sapphire substrate is defined by the bottom layer of the unit cell, as specified in the standard crystallographic information (cif) file. See figure captions of **Figure 2c**. (b) DFT calculation of the adsorption energy as a function of different twisted angles between MoS_2 and sapphire substrate. In this calculation, to neglect the ambiguity in the atomic configuration of MoS_2 domain edge, it is assumed that commensurate infinite monolayer MoS_2 slabs adsorbed with different twisted angles on c-plane sapphire of stoichiometric single-Al-terminated surface, which has been reported most energetically stable.[20,21]

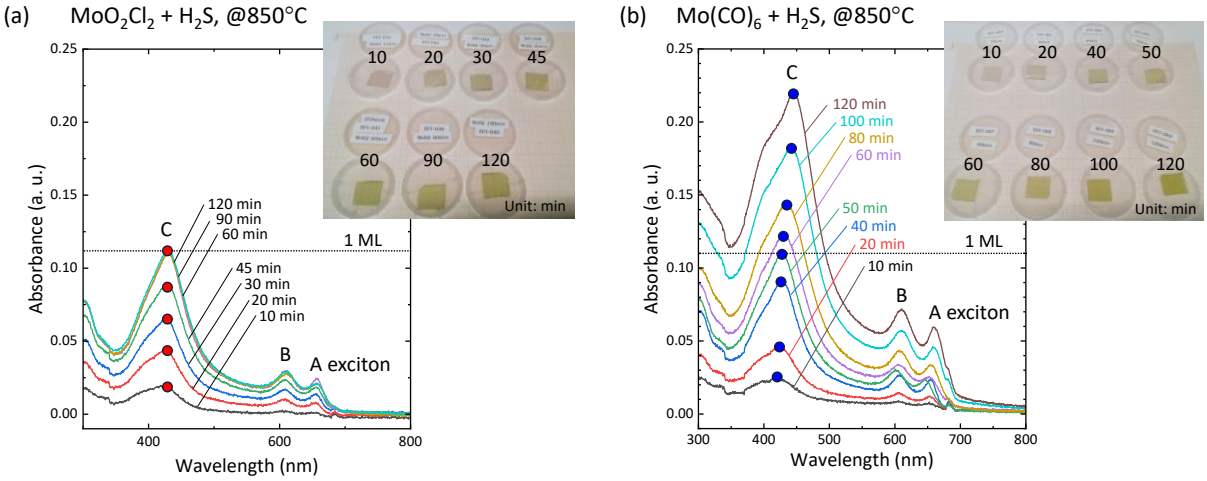

Figure S16 Absorbance spectra of MoS_2 films grown on sapphire substrates for various growth times using (a) MoO_2Cl_2 and H_2S precursors and (b) $Mo(CO)_6$ and H_2S precursors. The characteristic A, B, and C excitonic peaks are observed. Notably, double-side-polished sapphire substrates were employed for these absorbance measurements. The insets display photographs of MoS_2 films on sapphire substrates at different growth times. For the $Mo(CO)_6$ precursor, the darkness of the sapphire substrates increases with extended growth time, while for the MoO_2Cl_2 precursor, it saturates at 60 minutes, demonstrating the self-limited layer-controlled synthesis.

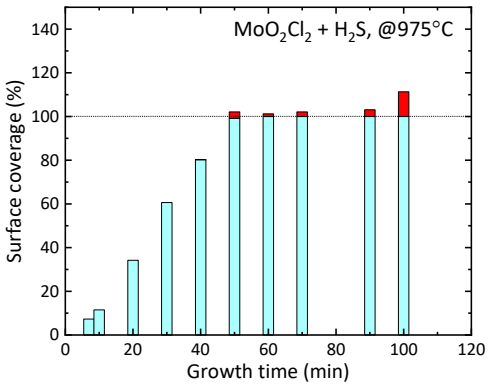

Figure S17 Surface coverage of monolayer MoS_2 grown at 975°C on sapphire substrates using MoO_2Cl_2 and H_2S precursor gases, as was determined from AFM analysis (**Figure 3b**) and SEM. This data suggests that profound self-limiting growth behavior at an elevated temperature of 975°C.

Note: The observed self-limiting growth mechanism is ascribed to the site-selective adsorption behavior of the MoO_2Cl_2 precursor. The proposed scenario is as follows: MoO_2Cl_2 exhibits a strong preferential adsorption onto the dangling bonds of the sapphire substrate surface, while displaying markedly limited interaction with the chemically inert surface of monolayer MoS_2. This selective adsorption behavior likely inhibits further nucleation of a second MoS_2 layer by the reaction with H_2S. In contrast, the $Mo(CO)_6$ precursor appears to nucleate the second layer regardless of the underlying surface inertness of MoS_2. This distinction is also reflected in the time-resolved in-plane XRD spectra. As shown in **Figure 1c** and **Supplementary Fig. S5**, even after reaching complete monolayer coverage at 60 min, the primary diffraction peak at 0° exhibits no additional broadening, and the integrated intensity saturates. In contrast, in the case of $Mo(CO)_6$ precursor, the 0° peak displays a pronounced broadening at extended growth durations of 90 and 120 minutes, as detected in **Supplementary Fig. S8**. This phenomenon is ascribed to the mosaic spread introduced by a secondary epitaxial MoS_2 layer, which exhibits rather broad in-plane misalignment around 0°.

However, we hypothesize that this site selectivity of MoO_2Cl_2 may be disturbed by the presence of GBs. Unsaturated dangling bonds appear near GBs, and MoO_2Cl_2 may adsorb there and nucleate the second layer of MoS_2. This mechanism likely accounts for the subtle broadening observed in the XRD peak beyond 60 minutes of growth, as well as the slight appearance of 30° twisted domains in the spectrum acquired at 950 °C, as shown in **Supplementary Fig. S7**. In fact, AFM measurements revealed a higher density of second-layer islands in samples grown at 950 °C relative to those synthesized at 975 °C. To fully leverage the self-limiting characteristics for achieving uniform monolayer coverage, it is therefore imperative to facilitate the in-plane self-alignment of grains and prevent the formation of GBs, thereby preserving the intrinsic site-selectivity of the precursor–substrate interaction.

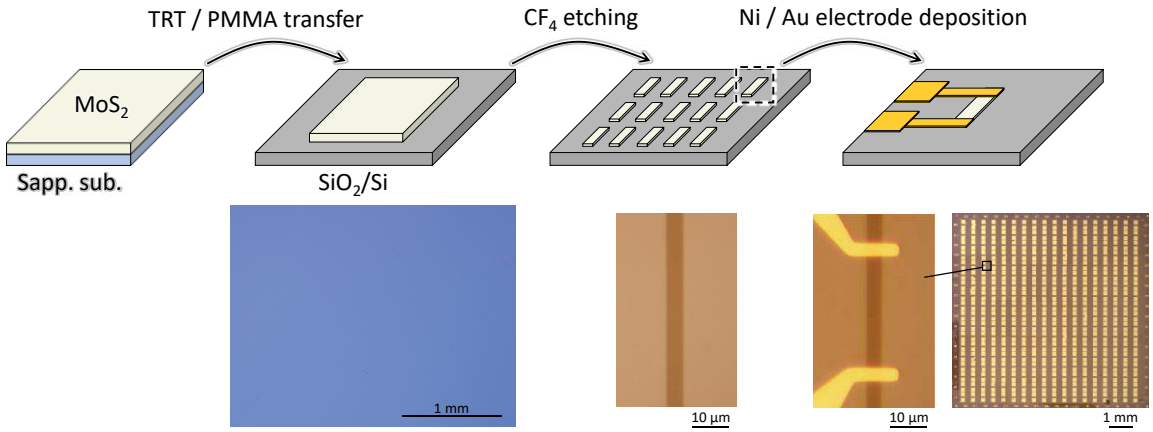

Figure S18 Schematic illustration of device fabrication process. First of all, monolayer MoS_2 grown on a sapphire substrate was transferred to a SiO_2/Si substrate.[22] The MoS_2 channel region was defined by CF_4 etching. Finally, Ni/Au electrode was formed for back gate MoS_2 FET.

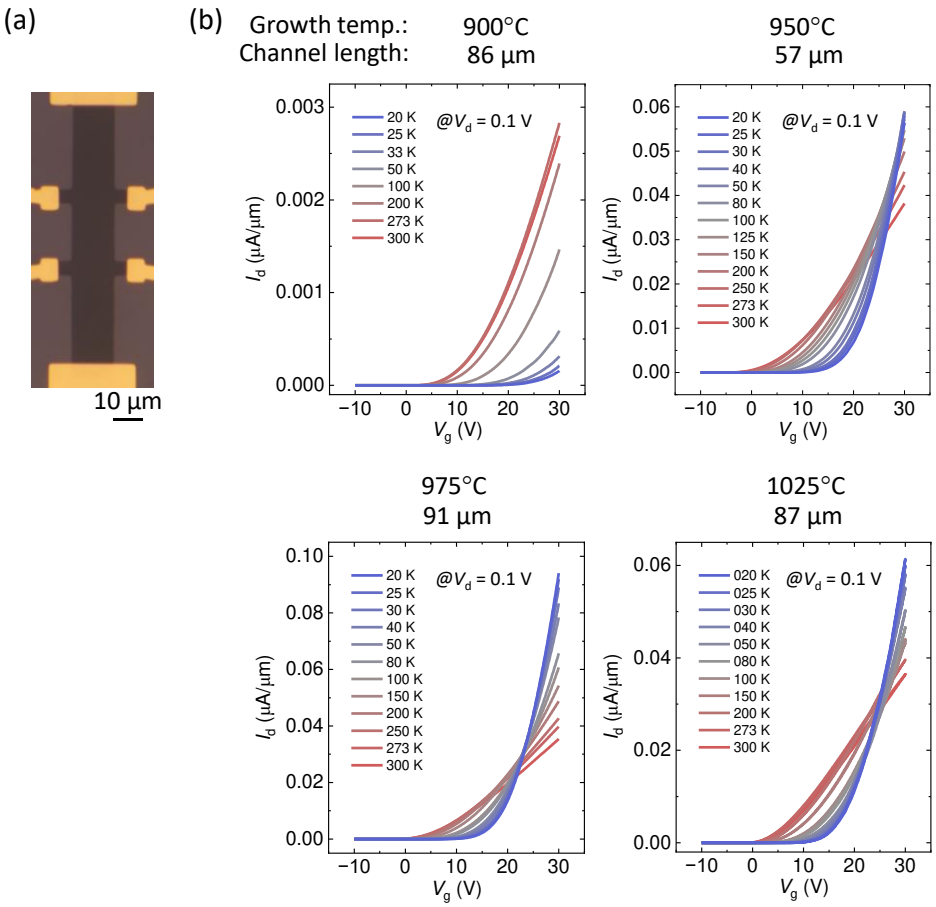

Figure S19 (a) Photograph of typical four probe device. (b) Two probe I_d-V_g curves at various temperatures for monolayer MoS_2 transferred onto SiO_2/Si substrate. The growth temperature and channel length are indicated at the top of figures.

References

1. Gäggeler, H. W. & Türler, A. *Gas-phase chemistry of superheavy elements*. (Springer, Berlin, Heidelberg, 2014).
2. Saeki, Y. & Matsuzaki, R. Thermochemical properties of molybdenum dioxydichloride. *Denki Kagaku oyobi Kogyo Butsuri Kagaku* **34**, 504–505 (1966).
3. Sato, T., Shibata, H., Hayashi, H., Takano, M. & Kurata, M. Chlorination of UO_2 and $(U,Zr)O_2$ solid solution using $MoCl_5$. *J Nucl Sci Technol* **52**, 1253–1258 (2015).
4. Ohta, T., Cicoira, F., Doppelt, P., Beitone, L. & Hoffmann, P. Static vapor pressure measurement of low volatility precursors for molecular vapor deposition below ambient temperature. *Chemical Vapor Deposition* **7**, 33–37 (2001).
5. Chubarov, M., Choudhury, T. H., Zhang, X. & Redwing, J. M. In-plane x-ray diffraction for characterization of monolayer and few-layer transition metal dichalcogenide films. *Nanotechnology* **29**, 055706 (2018).
6. Dumcenco, D. *et al.* Large-area epitaxial monolayer MoS_2. *ACS Nano* **9**, 4611–4620 (2015).
7. Deb, P. *et al.* Imaging polarity in two dimensional materials by breaking Friedel's law. *Ultramicroscopy* **215**, 113019 (2020).
8. Dosenovic, D. *et al.* Mapping domain junctions using 4D-STEM: toward controlled properties of epitaxially grown transition metal dichalcogenide monolayers. *2D Mater* **10**, 045024 (2023).
9. Psilodimitrakopoulos, S. *et al.* Optical versus electron diffraction imaging of twist-angle in 2D transition metal dichalcogenide bilayers. *npj 2D Mater Appl* **5**, 77 (2021).
10. Yin, X. *et al.* Edge nonlinear optics on a MoS_2 atomic monolayer. *Science (1979)* **344**, 488–490 (2014).
11. Ohtake, A., Suga, T., Goto, S., Nakagawa, D. & Nakamura, J. Atomic structure of the Se-passivated GaAs(001) surface revisited. *Sci Rep* **13**, 18140 (2023).
12. Rous, P. J. & Pendry, J. B. The theory of tensor LEED. *Surf Sci* **219**, 355–372 (1989).
13. Rous, P. J. *et al.* Tensor LEED: A technique for high-speed surface-structure determination. *Phys Rev Lett* **57**, 2951–2954 (1986).
14. Doucette, L. D., da Cunha, M. P. & Lad, R. J. Precise orientation of single crystals by a simple x-ray diffraction rocking curve method. *Review of Scientific Instruments* **76**, 036106 (2005).
15. Hong, J. *et al.* Atomistic dynamics of sulfur-deficient high-symmetry grain boundaries in molybdenum disulfide. *Nanoscale* **9**, 10312–10320 (2017).
16. Thompson, C. V. Grain growth in thin films. *Annu. Rev. Mater. Sci.* **20**, 245–268 (1990).
17. Thompson, C. V., Floro, J. & Smith, H. I. Epitaxial grain growth in thin metal films. *J Appl Phys* **67**, 4099–4104 (1990).
18. Nalin Mehta, A. *et al.* Grain-boundary-induced strain and distortion in epitaxial bilayer MoS_2 lattice. *The Journal of Physical Chemistry C* **124**, 6472–6478 (2020).
19. Ly, T. H. *et al.* Misorientation-angle-dependent electrical transport across molybdenum disulfide grain boundaries. *Nat Commun* **7**, 10426 (2016).

20. Godin, T. J. & LaFemina, J. P. Atomic and electronic structure of the corundum (α-alumina) (0001) surface. *Phys Rev B* **49**, 7691–7696 (1994).
21. Wang, X.-G., Chaka, A. & Scheffler, M. Effect of the Environment on α-A_2O_3 (0001) Surface Structures. *Phys Rev Lett* **84**, 3650–3653 (2000).
22. Kim, H., Ovchinnikov, D., Deiana, D., Unuchek, D. & Kis, A. Suppressing nucleation in metal-organic chemical vapor deposition of MoS_2 monolayers by alkali metal halides. *Nano Lett* **17**, 5056–5063 (2017).